UC Berkeley

UC Berkeley Electronic Theses and Dissertations

Title

Distributed Pressure Sensing for Chord Control of Airplane Roll

Permalink

https://escholarship.org/uc/item/69n6q3hz

Author

Holda, Conrad Adam

Publication Date

2022

Peer reviewed|Thesis/dissertation

eScholarship.org Powered by the California Digital Library
University of California

Distributed Pressure Sensing for Chord Control of Airplane Roll

by

Conrad Adam Holda

A dissertation submitted in partial satisfaction of the

requirements for the degree of

Doctor of Philosophy

in

Engineering - Mechanical Engineering

in the

Graduate Division

of the

University of California, Berkeley

Committee in charge:

Professor Ronald S. Fearing, Chair
Professor Francesco Borrelli, Co-chair
Professor Kameshwar Poolla
Professor Claire Tomlin

Summer 2022

Distributed Pressure Sensing for Chord Control of Airplane Roll

Copyright 2022
by
Conrad Adam Holda

Abstract

Distributed Pressure Sensing for Chord Control of Airplane Roll

by

Conrad Adam Holda

Doctor of Philosophy in Engineering - Mechanical Engineering

University of California, Berkeley

Professor Ronald S. Fearing, Chair

Professor Francesco Borrelli, Co-chair

Comparing airplanes to birds, there is a considerable difference in the way each achieves flight. Airplanes are rigid structures with a few sensors and actuators placed in optimized spots on the structure. Birds, on the other hand, use biological sensors throughout their bodies as well as are able to contort their wings and body to get the desired effects to fly. In this dissertation, I introduce a novel method inspired by birds for achieving controlled flight of an airplane.

First, I look at the wing in spanwise discretized sections. Each section can be analyzed as an airfoil and has a set of pressure sensors to retrieve aerodynamic parameters: angle of attack and freestream velocity. Three methods to retrieve these parameters are evaluated for accuracy and computation speed. The best method is chosen for the remainder of this dissertation. Additionally, each section has a flap that can alter the lift, drag and pitching moment resulting from the airflow going over the section. I propose an attitude control loop to integrate the new knowledge of the localized airflow of each wing section across the entire wing to more optimally move the actuators and meet the desired attitude.

Subsequently, I demonstrate the proposed distributed sensing and control method working through tests on the roll dynamics of a wing. These tests show that the new method proposed in this dissertation detects localized airflow that would not be noticed by traditional sensing methods, follows a reference roll signal in a nominal condition more efficiently, and better rejects localized airflow disturbances.

Lastly, I present a novel design for sensitive thin-film capacitive pressure sensors that can be distributed across aerodynamic surfaces without the need of embedding pressure sensors into the wing structure.

This dissertation is dedicated to my wife, Samantha.

Contents

List of Figures

List of Tables

Acknowledgments

First and foremost, I would like to thank professor Ronald Fearing, my advisor, who provided me guidance and the freedom to explore topics that seemed meaningful to me. Additionally, thank you for not giving up on my projects when, at the time, they seemed impossible to me, but turned out to be a minor hiccup in the process. I'd also like to thank my co-advisor, Francesco Borrelli. I know your schedule is hectic but when needed, I was able to borrow some of your time.

Next, I'd like to thank my dissertation committee, professors Kameshwar Poolla and Claire Tomlin, and my qualifying exam committee, professors Anil Aswani, Mark Mueller, Kameshwar Poolla, and Claire Tomlin.

Thanks to members of the Biomimetic Millisystems Lab: Sareum Kim, Anusha Nagabandi, Xinlei Pan, Eric Wang, and Justin Yim. Friday coffee hours, lunches, and being one of the first to see your robots work was always something to look forward to.

Thanks to my friends. Monimoy Bujarbaruah and Saman Fahandezh-Saadi thanks for the endless humor, and reminders that the American diet is far from ideal. Oscar Rios, I view you as a mentor, you were the first person I saw go through the PhD process and inspired me to get one. I tried to be the TA to my students that you were to me. Oliver Sumo, thank you for keeping me accountable and forcing me to workout. You better not stop either, my watch notifications will snitch - no excuses are allowed!

Now to thank my family, without which I have no doubt that I would have not completed my studies. Samantha, I believe the amount of work you put in to help me (from editing my writing, to running through ideas to fix issues, asking coworkers at Boeing aerodynamic questions, etc...), you should be getting this degree as well. You also helped me take much needed breaks and planned most, if not all, of the vacations I took throughout my PhD. My parents and sister, thank you for providing me with spare hands when conducting tests at home, and letting me claim arbitrary items (mom, your cherished e-bike was pivotal to the work presented in Chapter 4) from our home that could be useful in my research. Your enthusiasm for my projects, which you knew little about, also helped propel me to get them working.

Chapter 1

Introduction

Flying robots and vehicles are common in many present-day applications. These robots and vehicles typically rely on internal sensors to estimate their state. Real world disturbances, such as wind gusts, are rejected using centralized sensors with these traditional sensors and control schemes.

In the natural world, flying animals and insects do not rely on only internal sensors, rather, they also use a network of biological distributed exteroceptive sensors. For example, insects have small wind-sensitive hairs located on their wings and birds have feathers attached to their muscles which allows them to sense wing loading [22, 23, 24]. A variety of sensors have been created to mimic these biological sensing features, such as whisker and hair inspired sensors. These sensors have been introduced to directly measure airflow from the amount of whisker or hair deflection [17, 21, 22]. Fish also rely on their distributed biological sensors to sense the flow of water around them. The lateral line is a system of sensory organs distributed down the length of their bodies used to detect movement and pressure gradients as they swim through water. These lateral line organs have been mimicked through the creation of line pressure arrays, which are used on fish-like robots to better detect and reject flow disturbances in the water [18, 30]. Just as in these fish, pressure sensor arrays can be used to sense airflow over wings on airplane.

As air flows over aerodynamic surfaces, it produces a pressure distribution as described by Bernoulli's equation [3]. Measuring this pressure distribution can lead to a better understanding of the airflow across the surface. The design of a pressure sensor array measuring the pressure distribution on a surface must take into consideration the resolution of the particular aerodynamic surface being observed. For example, a butterfly has a pressure differential on its wings on the order of Pascals [36] whereas a Horstmann and Quast HQ17 airfoil wing section traveling around 170 m/s has a pressure distribution on the order of 100's of Pascals [20]. Researchers have used measurements of the pressure distribution to retrieve airflow parameters in [8, 9]. With a distributed pressure sensor system, localized airflow disturbances can be observed. For example, if a vortex disturbance is encountered, a distributed pressure sensor array placed on the wing can sense this local occurrence, allowing for an effective control system action to mitigate the effect of the vortex. A control

Figure 1.1: A radio controlled airplane with a span of 1.1 m.

response based only on an IMU, on the other hand, may be less appropriate as it will have less information on the airflow over potentially stalled control surfaces.

In addition to sensing the pressure distribution to retrieve an estimate of the airflow, nature's flyers have wings that contort into various shapes to obtain the flyer's desired attitude. The way wings deflect are not very similar to how today's conventional airplanes actuate their aerodynamic surfaces - most conventional airplanes use a few discrete actuators to change the aerodynamic forces and moments. Flying robots have also been implemented with wing motions similar to those of nature. These robots are equipped with bat-like flapping wings that allow such flyers to do various maneuvers not possible with traditional airplanes [26, 29]. Additionally, researchers have explored the possibility of having continuous flaps rather than having a section of wing move on a pivot or hinge. The benefits can include

Pressure Sensor Type	Total Sensors	Actuators	Reference
Capacitive, Differential	4	-	[9]
COTS, Differential	4	-	[13]
COTS, Absolute	7	1 (angle of attack control)	[39]
COTS, Absolute	9	1 (simulated pitch control)	[35]
COTS, Absolute	42	3 (simulated attitude control)	[34]
COTS, Absolute	64	8 (roll control)	This work

Table 1.1: Representative airflow sensing using pressure sensors. Two previous explorations into airflow sensing also simulated control using the new information. The total sensors section counts the number of pressure sensors used to measure the static pressure of aerodynamic surfaces, and did not include the sensors used to measure a reference pressure. The actuators section counts the number of actuators that used the new airflow information for control.

more effective actuators [19], and more efficient flight by the reduction of drag [2].

In this dissertation, a distributed pressure sensor array is implemented to mimic nature and to allow a novel controller to gain a better understanding of the localized airflow about a wing. Table 1.1, shows relevant previous works that used distributed pressure sensors to estimate localized airflow, three of which also implemented control techniques utilizing the airflow estimates. Callegari et al used capacitive differential pressure sensors and a least squares approach to retrieve the angle of attack and velocity of a wing in wind tunnel tests [9]. Gavrilovic et al used COTS differential pressure sensors measuring the pressure difference between the top and bottom of a wing to retrieve those parameters as well. The data was then verified through flight tests using an angle of attack vane and pitot tube [13]. Wood et al showed a neural network was able to determine the angle of attack and airspeed which was used in a closed-loop controller to track a reference angle of attack signal. The neural network was trained on data gathered from wind tunnel tests and outdoor flight tests [39]. Shen et al verified the airflow parameters in a wind tunnel and successfully simulated the attitude control of a wing and an airplane using the information about the airflow with a traditional airplane actuator layout [35, 34].

The contributions of this dissertation that are presented and validated use a different approach where independent actuators are also distributed to control the roll angle. A wing, similarly sized to the wing mounted on the airplane pictured in Figure 1.1, is discretized into sections, so that the pressure sensor array is used to retrieve the localized, 2 dimensional aerodynamic parameters of angle of attack and freestream velocity for thin strips of a wing. Retrieving the angle of attack and freestream velocity parameters from the thin wing section, an airfoil, with the use of pressure sensors is compared with three methods. The best of these methods is used for the rest of the dissertation. The method is also thoroughly tested in a wind tunnel. Each of the thin strips of wing is equipped with individual flaps and combined into a complete wing. The distributed flaps allow the centralized flight controller to optimally shape the wing to get the desired attitude of the wing. The flap deflections may be closer to that of a wing found in nature than that of a conventional airplane with traditional control surfaces. Lastly, a sensitive, thin-film capacitive pressure sensor array is explored to allow for topical application of sensors to a wing. This potential array can be used for the distributed pressure array while improving the design of the wing so no pressure sensors would have to be embedded inside the wing structure.

1.1 Outline

Chapter 2 will explore the retrieval of the aerodynamic parameters, angle of attack and freestream velocity, for an airfoil. Chapter 3 will show experiments conducted in a wind tunnel to retrieve the aerodynamic parameters for an airfoil using consumer off-the-shelf (COTS) pressure sensors. Chapter 4 will introduce a new control method that utilizes distributed COTS pressure sensors to optimally control an airplane and is proven by a few tests. Chapter 5 will look at sensitive thin film capacitive pressure sensor design to be applied to aerodynamic surfaces.

Chapter 2

Retrieving Aerodynamic Parameters using Distributed Pressure Sensors along a Chord

As air flows across a shape, it can speed up or slow down as it conforms to the shape. This change in the flow imparts a force on the shape from both the shear stress and the pressure distribution on the surfaces. The pressure distribution is determined by the speed of the air flowing over the particular section. The faster the air is moving over the section the lower the pressure will be at that section. This phenomena is described by Bernoulli's equation [3]:

$$p_{\text{total}} = p_{\text{static}} + p_{\text{dynamic}} \tag{2.1}$$

The total pressure of the air is the sum of the static pressure, the pressure on the surface producing the pressure distribution, and the dynamic pressure. The dynamic pressure is computed from the velocity of the air, v_∞, and the density of the air, ρ:

$$p_{\text{dynamic}} = \frac{1}{2}\rho v_\infty^2 \tag{2.2}$$

Aerodynamicists have also found that the pressure distribution can be nondimensionalized for different shapes with respect to the static pressure and the dynamic pressure of the freestream air. The coefficient of pressure, representing the nondimensionalized static pressure, is given by:

$$\frac{p - p_\infty}{\frac{1}{2}\rho v_\infty^2} = C_p \tag{2.3}$$

where p is the static pressure at the given point, and p_∞ is the static pressure of the environment.

In aerodynamics, a 2-dimensional section of an aerodynamic surface designed for producing a lift force while minimizing a drag force is called an airfoil. The coefficient of pressure, and therefore the static pressure, varies along the airfoil, which can be denoted by the position, x. It also varies on how the airfoil is positioned with respect to the airflow, known as the angle of attack, α. In a viscid analysis, the coefficient of pressure distribution will also change relative to freestream velocity, v_∞. Whereas in an inviscid analysis, the coefficient of pressure distribution does not rely on freestream velocity. Thus, the coefficient of pressure for an inviscid analysis is a function of position and angle of attack, $C_p(x, \alpha)$, while for a viscid analysis the coefficient of pressure also depends on freestream velocity, $C_p(x, \alpha, v_\infty)$.

Assuming the shear stress imparted by the flow on the airfoil is small, an inviscid analysis can be used to compute the pressures on the surface of the airfoil. Therefore, the forces and moments on the airfoil can be computed by integrating the pressure distribution over its surface. Instead, if shear stresses are not to be neglected, a viscid analysis should be used. In this case the forces and moments can be computed by integrating the pressure and shear distributions. These forces and moments on the airfoil from the freestream are known as the lift, drag and pitch moment. Additionally, when using a viscid analysis, airflow separation from the airfoil can be recreated which results in a drastic drop off in lift as the angle of attack becomes too aggressive. In an inviscid analysis, this phenomena is not observed which results in some inaccuracies.

2.1 Sensitivity of Aerodynamic Parameters with Respect to Pressure

A pressure sensor can measure the static pressure at a point on the airfoil with some noise, σ. The sensor equation is modeled by the coefficient of pressure and the velocity of the freestream air velocity.

$$s = \frac{1}{2}\rho v_\infty^2 C_p + p_\infty + \sigma \tag{2.4}$$

The error of the sensor can cause retrieving the airflow parameters to stray from their true values, thus it is useful to determine the sensitivity of such parameters with respect to the sensor noise.

The following sensitivity analysis is of an airfoil that uses an inviscid assumption of the airflow and only contains a single sensor to determine either the airflow velocity or angle of attack. It is important to note, that both airflow velocity and angle of attack cannot be determined by one sensor.

2.1.1 Airflow Velocity Sensitivity

Rewriting the sensor equation, 2.4, to compute the airflow velocity exhibits a function of the sensor reading, the angle of attack, static pressure of the freestream airflow, and density of the air.

$$v_\infty = \sqrt{2\frac{s(x) - p_\infty}{\rho C_p(x, \alpha)}} \tag{2.5}$$

Adding the additional assumption of level flight, where air density is relatively constant, the sensitivity is proportional to the inverse of the airflow velocity for an inviscid analysis.

$$\frac{\partial v_\infty}{\partial s(x)} = \frac{2}{\rho C_p(x,\alpha)} \left(2\frac{s(x) - p_\infty}{\rho C_p(x,\alpha)} \right)^{-1/2} = \frac{2}{\rho C_p(x,\alpha) v_\infty} \propto \frac{1}{v_\infty} \tag{2.6}$$

This result shows that the accuracy of a static pressure sensor used to determine the airflow velocity is more critical at lower velocities.

A common RC airplane, as in Figure 1.1, flying in a park approximately ranges in velocities from 5 m/s to 15 m/s. At its lower velocities, the same error in static pressure reading as the airplanes higher speeds will result in three times worse estimates of the airspeed. The inverse relation between velocity and the sensitivity is described in Figure 2.1, when $\rho C_p(x,\alpha)$ is equal to 2.

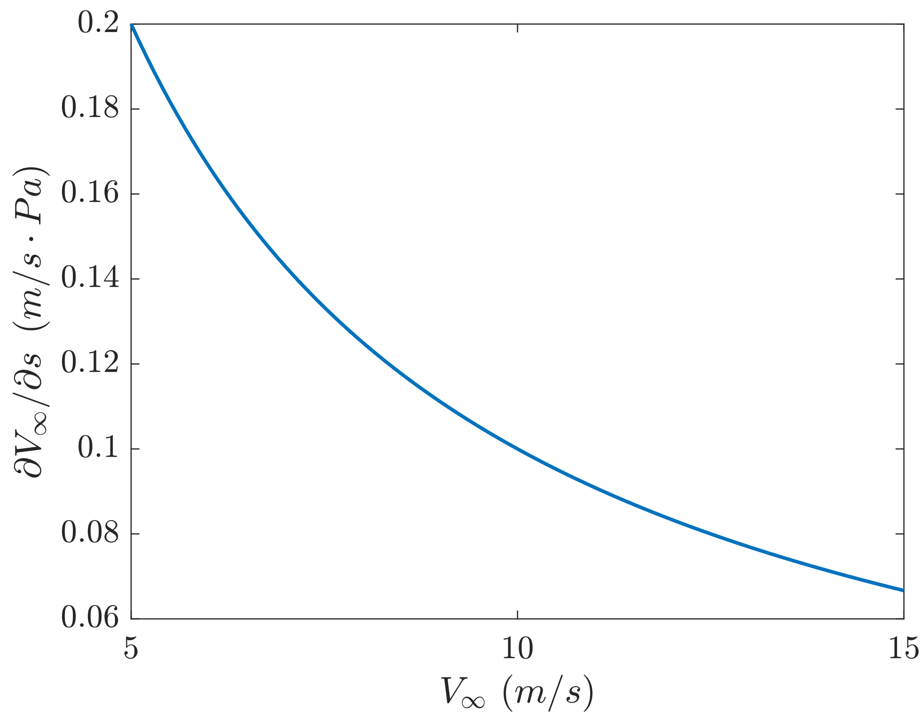

Figure 2.1: The sensitivity relationship between static pressure anywhere on the airfoil with respect to freestream velocity, when $\rho C_p(x,\alpha)$ is equal to 2.

2.1.2 Angle of Attack Sensitivity

Looking at the sensitivity of retrieving the angle of attack with respect to the static pressure sensor error, the relation is not as obvious. Angle of attack affects the the sensor equation, 2.4, by changing the coefficient of pressure. The coefficient of pressure is determined experimentally or with the use computational fluid dynamics. To get the sensitivity of the angle of attack, the chain rule must be implemented

$$\frac{\partial C_p(x,\alpha)}{\partial s(x)} = \frac{\partial \alpha}{\partial s(x)} \frac{\partial C_p(x,\alpha)}{\partial \alpha} \tag{2.7}$$

Mitigating the need to differentiate large differential equations, $\partial C_p/\partial\alpha$ was estimated from XFOIL [10]. The estimates from XFOIL were computed using inviscid assumptions due to the fact that the viscous analysis resulted in non-smooth derivatives of the coefficient of pressure with respect to angle of attack.

$$\frac{\partial \alpha}{\partial s(x)} = \frac{1}{\frac{\partial C_p}{\partial \alpha}} \left(\frac{2}{\rho v_\infty^2}\right) \tag{2.8}$$

It is apparent that the sensitivity equation is not as simple as in the previous case. The sensitivity relies on airflow velocity, angle of attack, and position of the pressure sensor on the airfoil.

Again, looking at the RC airplane in Figure 1.1 and assuming a NACA 2412 airfoil for the airplane's main wing, the sensitivity of the angle of attack can be observed in Figure 2.2. As the position on the airfoil and freestream velocity change, the sensitivity of angle of attack with respect to pressure change. The plots show 5 different locations at two freestream velocities. This result - sensors near the rear of the airfoil are more sensitive - is as expected from looking at the coefficient of pressure distribution along the airfoil as the angle of attack varies. As seen in Figure 2.3, the rear of the airfoil has a smaller coefficient of pressure change across all angle of attack. In comparison, the front of the airfoil coefficient of pressure values vary more as the angle of attack is altered.

Additionally, an inverse relationship is also noticed with the sensitivity as the airflow These results mean that the optimal aerodynamic parameter retrieval will occur at faster freestream velocities as well as sensors near the leading edge. This was also theorized in previous works, where sensors were placed near the leading edge had better airflow estimation of the angle of attack [40].

2.2 Least Square Approach to Retrieve Angle of Attack and Freestream Velocity

As noted earlier, one pressure sensor is not adequate to retrieve both aerodynamic parameters: angle of attack and freestream velocity. At least two static pressure measurements are needed; however, more will help address the issue of sensor noise. Using more than 2 sensors will also result in an over determined system, so a method to reduce the error of the aerodynamic parameter estimations needs to be implemented.

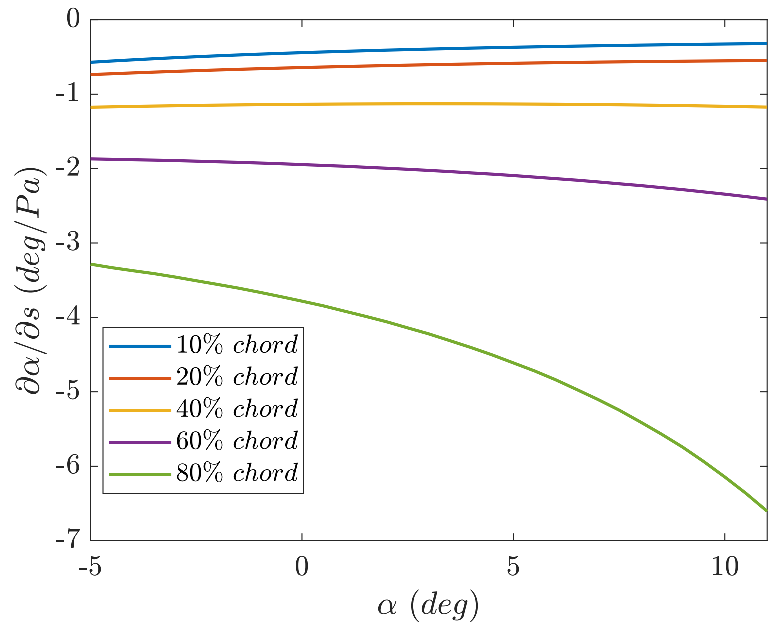

(a) $v_\infty = 5\ m/s$

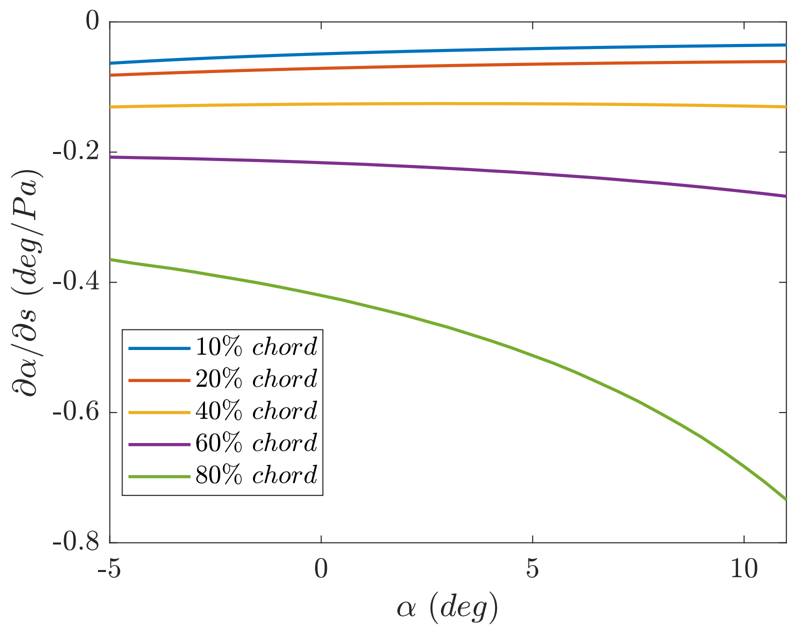

(b) $v_\infty = 15\ m/s$

Figure 2.2: Sensitivity with respect to angle of attack for an inviscid model at 5 locations on a NACA 2412 airfoil. (a) Shows sensitivity when the airflow is at 5 m/s. (b) Shows sensitivity when the airflow is at 15 m/s.

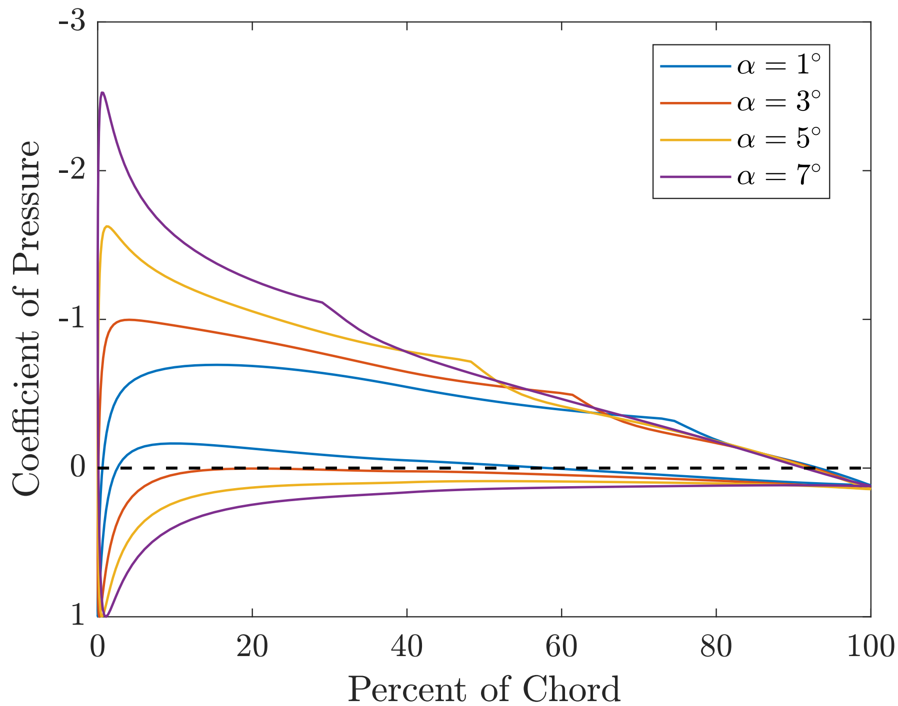

Figure 2.3: Coefficient of pressure on the airfoil as angle of attack is varied from 1° to 7°.

The first method that can be used to retrieve the aerodynamic parameters is by least square minimization as done by S. Callegari, et al [9]. Writing out the minimization of the error between measured static pressure of the sensor array and the estimated static pressure array:

$$\begin{aligned} &\min_{\alpha, v_\infty} \|\mathbf{s} - \frac{1}{2}\rho v_\infty^2 C_p + p_\infty \mathbf{1}\|_2^2 \\ &\text{s.t. } v_\infty \geq 0 \end{aligned} \tag{2.9}$$

The freestream velocity must be bounded because the airfoil will be assumed to be going forward and the coefficient of pressure will only be computed by XFOIL going forward, not backward. Additionally, the coefficient of pressure can either be computed using an inviscid analysis or a viscid analysis. For this method in this dissertation, a viscid analysis was used to better estimate conditions near stall. To solve the minimization, a descent method can be used due to the nonlinearity of the coefficient of pressure, C_p.

2.3 Kalman Filter Approach to Retrieve Angle of Attack and Freestream Velocity

Without weights the least squares approach does not take into consideration the varying sensitivity with respect to sensor position on the airfoil. To optimally weigh the sensors, a Kalman Filter can be used. A Kalman Filter will also leverage previous sensor readings to generate a better estimate of the aerodynamic parameters, whereas the least squares approach only considers the current sensor readings.

A 0-dynamics model is used with additive disturbance for the dynamics model:

$$\begin{bmatrix} \alpha(k) \\ v_\infty(k) \end{bmatrix} = \begin{bmatrix} \alpha(k-1) \\ v_\infty(k-1) \end{bmatrix} + \mathbf{v}(k-1) \tag{2.10}$$

whereas there are two options for the sensor model. The first option is using an inviscid sensor model for the coefficient of pressure:

$$\mathbf{s}(k) = h(\alpha(k), v_\infty(k), \mathbf{w}(k)) = \frac{1}{2}\rho v_\infty^2(k) C_p(\mathbf{x}, \alpha(k)) + \mathbf{w}(k) \tag{2.11}$$

and the second option is using a viscid sensor model:

$$\mathbf{s}(k) = h(\alpha(k), v_\infty(k), \mathbf{w}(k)) = \frac{1}{2}\rho v_\infty^2(k) C_p(\mathbf{x}, \alpha(k), v_\infty(k)) + \mathbf{w}(k) \tag{2.12}$$

Both sensor models assume additive sensor noise. Additionally, for this dissertation, the additive model disturbance and sensor noise are assumed to be independent.

The sensor model is nonlinear from the coefficient of pressure function. An Extended Kalman Filter (EKF) or an Unscented Kalman Filter (UKF) can be used to deal with the nonlinearity. The EKF, however, relies on the Jacobian of the sensor model, so the EKF should only be used if using an inviscid analysis for the coeffienct of pressure as the viscid analysis does not have well behaved derivatives. This means the EKF will not do well recovering aerodynamic parameters in extreme scenarios such as stall and should be relegated to typical flow regimes away from airflow separation. The UKF has no such restriction as it does not rely on derivatives of the coefficient of pressure, so the coefficient of pressure was determined via viscid analaysis.

2.4 Simulations

Simulations were conducted to compare the 3 methods of retrieving aerodynamic parameters. The methods were then compared using two criteria: speed of determining an estimate and estimate accuracy. The first criteria is necessary if the particular approach will be used for real time aerodynamic parameter sensing (and control). The second criteria is useful, not only for accurate measurements, but also the ability to relax the pressure sensor resolution requirements resulting in a larger variety and/or cheaper pressure sensors that could be utilized.

2.4.1 Simulations in nominal operating conditions

First, the approaches were simulated for a set of aerodynamic parameters away from airflow separation of a NACA 2412 airfoil at 5° angle of attack and 10 m/s freestream velocity. The simulations have 5 sensors located at 10%, 20%, 40%, 60%, and 80% of the chord, each sensor has a zero mean noise of with a standard deviation of 5 Pa, making the additive sensor model noise $\mathbf{w} \sim \mathcal{N}(0\ Pa, 25I\ Pa^2)$.

100 steps were simulated. All 3 approaches used the same additive noise inputs. The simulations were conducted in Matlab on a Dell XPS 15 with an Intel i7-11800H CPU.

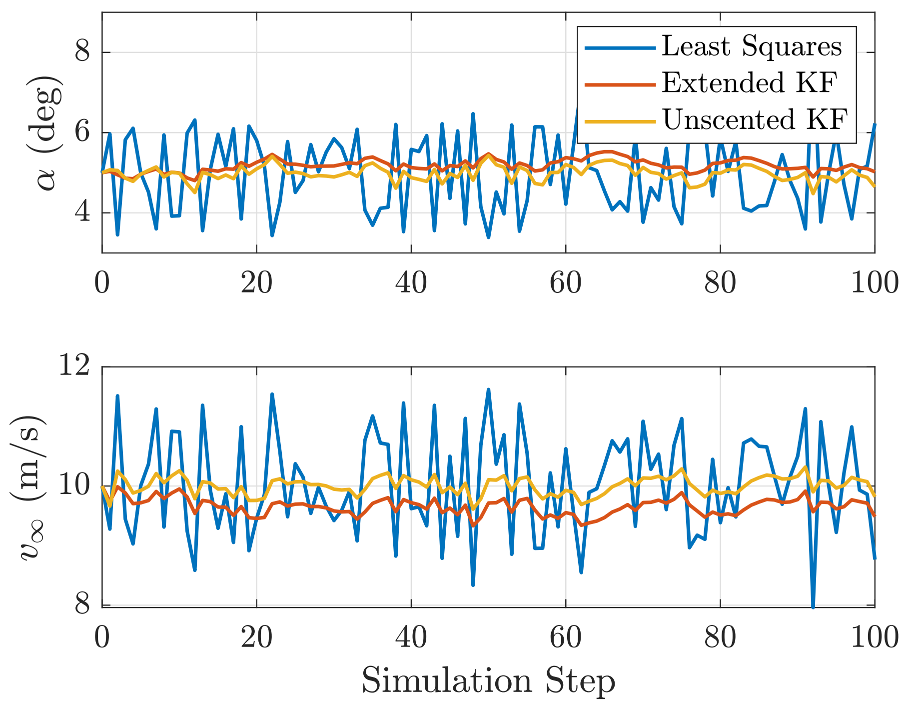

Figure 2.4: Comparison of the 3 methods to retrieve aerodynamic parameters of 5° angle of attack and 10 m/s freestream velocity where the pressure sensors had noise characterized by a normal distribution with a 5 Pa standard deviation.

Method	Avg α	Avg v_∞	Avg Time
Least Squares	$4.98° \pm 0.99°$	10.04 ± 0.84 m/s	33.6 ms
Extended KF	$5.18° \pm 0.15°$	9.66 ± 0.14 m/s	0.7 ms
Unscented KF	$4.98° \pm 0.18°$	10.01 ± 0.15 m/s	1.1 ms

Table 2.1: Comparison of methods to retrieve aerodynamic parameters at a nominal flight condition of 5° angle of attack and 10 m/s freestream velocity.

From the results, it can be seen that all three approaches seemed to get reasonably close to the actual aerodynamic parameters of 5° angle of attack and 10 m/s freestream velocity. However, the Least Squares approach had the greatest variance as well as took the longest time to compute an estimate - over one magnitude longer than the other two approaches. The EKF seemed to perform the best as it was the fastest and the accuracy seemed comparable to the UKF, while seeing slightly less variance than the Least Squares approach. This is as expected as the Kalman Filter approaches use the history of the past sensor readings as well as uses an optimal weight by the knowledge of varying sensitivity of sensor position.

2.4.2 Simulations near airflow separation

Next, a set of aerodynamic parameters near airflow separation were simulated with an angle of attack of 12° and freestream velocity of 10 m/s. The rest of the simulation variables remained the same.

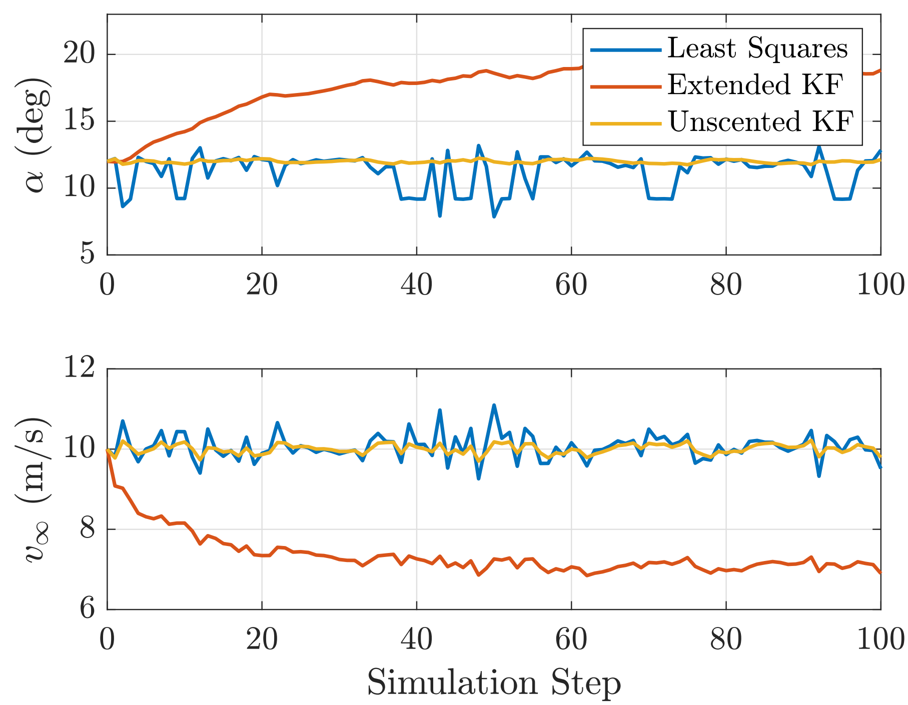

Figure 2.5: Comparison of the 3 methods to retrieve aerodynamic parameters of 12° angle of attack and 10 m/s freestream velocity where the pressure sensors had noise characterized by a normal distribution with a 5 Pa standard deviation.

From these results, a slightly different outcome was obtained when compared to the nominal case where stall was not an issue. The EKF clearly had the largest error in both estimates, whereas the Least Squares approach and UKF seemed to be able to more accurately

Method	Avg α	Avg v_∞	Avg Time
Least Squares	$11.28° \pm 1.31°$	10.06 ± 0.32 m/s	32.2 ms
Extended KF	$17.52° \pm 1.89°$	7.36 ± 0.51 m/s	0.7 ms
Unscented KF	$11.99° \pm 0.12°$	10.01 ± 0.12 m/s	1.1 ms

Table 2.2: Comparison of methods to retrieve aerodynamic parameters at a flight condition close to stall at 12° angle of attack and 10 m/s freestream velocity.

estimate the actual aerodynamic parameters. This stems from the fact that the EKF had to rely on the derivatives from an inviscid analysis that cannot predict stall. The remaining parameters seem to carry over from the previous simulations. The Least Squares approach had the highest variance and took the most time to compute, while the EKF approach was marginally faster than the UKF approach.

2.5 Concluding Remarks

Static pressure measurements at known points on an airfoil can be used to determine the angle of attack as well as the freestream velocity of the airfoil. From the discussion in this chapter, it can be seen that these pressure measurements are more tolerant to errors or noise the faster the freestream velocity is and the closer these measurements are taken to the leading edge of the airfoil. These observations can, therefore, help in the placement of pressure sensors on an airfoil and dictate what velocity would result in optimal retrieval of the aerodynamic parameters if needed for control of an aircraft.

Additionally, 3 approaches were benchmarked to compare how each performed for two regimes: a nominal case where separation is not expected, and an aggressive case where separation and stall dynamics of the airfoil are close. Overall, the Unscented Kalman Filter approach proved to do the best in both cases. The UKF was relatively quick to compute the angle of attack and freestream velocity while still retaining accuracy in both benchmark cases. Better accuracy can also be achieved if the 0-dynamics model is replaced with a more realistic dynamics model of the airfoil. An example can be if on an airplane, the dynamics model can utilize the difference of the pitch angle and flight path angle of the airplane to give an a priori estimate of the angle of attack.

Failure of sensors can also be an issue in retrieving aerodynamic parameters. There are a plethora of ways a pressure measurement can be inaccurate. The rudimentary case of sensor noise was addressed in the three methods; however, large errors, from sensors failures, can skew the retrieval of aerodynamic parameters. An algorithm can be adapted to ignore specific sensors if their readings are considerably far from the distribution the UKF predicts.

Chapter 3

Retrieving Aerodynamic Parameters in Wind Tunnel Experiments using COTS Pressure Sensors

3.1 Retrieving Aerodynamic Parameters

Most COTS pressure sensors are factory calibrated. However, these pressure sensors may potentially lose calibration through shipping, soldering and handling. Thus, small pressure errors may occur. It was noticed that the changes in pressures were relatively accurate, but there were small offset errors present. These offsets can be negated by subtracting an average upon startup; however, this results in the sensor reading the relative static pressure compared to the averaged static pressure upon board startup. This is shown by the relation:

$$s_i = p_i - p_\infty \tag{3.1}$$

Combining the new pressure measurement of relative static pressure with the analysis presented in Chapter 2, the sensor reading with respect to position on the airfoil, angle of attack, and freestream velocity becomes:

$$s_i = \frac{1}{2}\rho v_\infty^2 C_P(x_i, \alpha, v_\infty) + \sigma \tag{3.2}$$

Using this new sensor model, the Unscented Kalman Filter can still be used to retrieve the angle of attack and the freestream velocity of the airfoil.

3.2 Experimental Setup

Experiments were conducted inside an Eiffel style wind tunnel. Designed by Engineering Laboratory Design Inc., the wind tunnel was an open-circuit design with a 6.25 to 1 contraction section. The working section of the wind tunnel was 45.5 cm $\times$ 45.5 cm $\times$ 91.5 cm.

In addition, the wind tunnel had a controller regulating the frequency of the suction fan; depending on the environmental parameters (i.e. temperature of the room) the frequency of the suction fan could be mapped to an airflow velocity.

To calibrate the airflow velocity, a TSI VelociCalc 8346 anemometer was used which related the frequency of the suction motor to airflow velocity. The anemometer's data sheet states that the measurement is accurate to within 3% or 0.015 m/s, whichever is larger. [38]

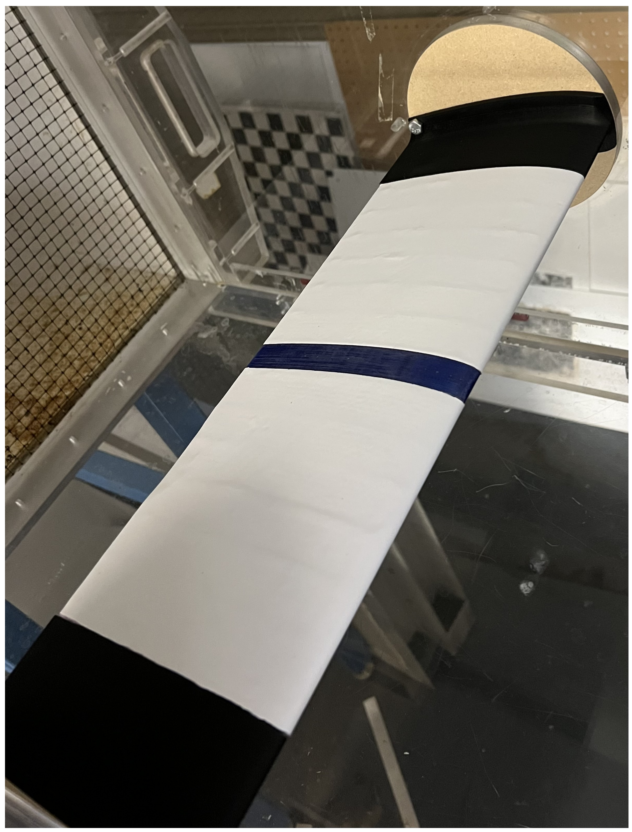

Figure 3.1: The wind tunnel setup of a wing with a NACA 2412 airfoil.

The wing tested used a NACA 2412 airfoil with a chord section of 15 cm and is pictured in Figure 3.1. The wing spanned the entire 45.5 cm test section so that wingtip effects would not interfere with results. The wing was mounted to the port holes on the wind tunnel so that the section could be rotated and set at various angles of attack. The angle of attack measurements were denoted in 1 degree increments and the angle of attack of the airfoil was able to be set to an accuracy of 0.5°. A PCB was used inside a 0.05 mm layer line 3D printed airfoil section with 8 ports on top of the airfoil. The remainder of the section was constructed out of extruded polystyrene and covered in a vinyl material. The position of the ports were spread at the positions 5 mm, 10 mm, 15 mm, 20 mm, 73.8 mm, 86.3 mm, and 107.1 mm from the leading edge. The latter 4 pressure ports were positioned such that they would be able to detect airflow separation on the airfoil for angles of 3°, 4°, 5°, and 6°;

however, the resolution of the sensors was not sufficient to be able to detect separation. All 8 sensors were used to retrieve the aerodynamic parameters of angle of attack and freestream velocity.

3.2.1 COTS pressure sensor board layout

The PCB used in the wind tunnel tests was designed to measure static pressures along the airfoil. The board was also designed with future work in mind - it would eventually be used to actuate control surfaces via a PPM signal to a commercial RC hobby servo while sensing pressures to retrieve the aerodynamic parameters of the wing section. The board resulted in being 20 *mm* wide by 106 *mm* long and is pictured in Figure 3.2.

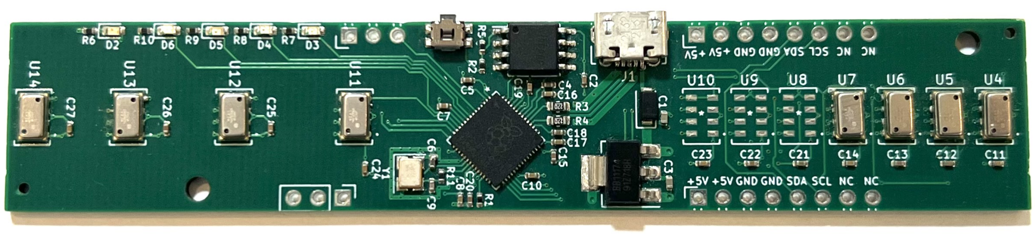

(a) Front of PCB

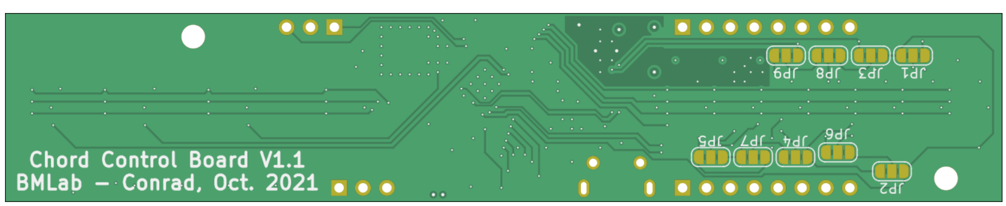

(b) Back of PCB (rendered)

Figure 3.2: The PCB inside the wing used to measure the relative static pressure at 8 points as well as compute the estimates for the angle of attack and freestream velocity onboard of its RP2040. The right side is closest to the leading edge when inside the wing, while the left side is closest to the trailing edge of the wing. Pressure sensor footprints U8, U9, and U10 were not populated. It contains capability to communicate to other boards via I2C and can actuate an RC servo via PPM.

Due to the presiding worldwide chip shortage, a limited selection of pressure sensors and MCU's were available to choose from.

The pressure sensors that were selected were TE's MS5607-02BA barometric pressure sensors [5]. These pressure sensors were selected because they are able to communicate via SPI, had decent resolution, and were available. It was important to select a chip that communicated via SPI as these sensors would be on the same communication bus, and sensors usually only have one or two addresses given by the manufacturer on other forms of communication (i.e. I2C). SPI allows for the MCU to communicate with a specific chip by driving the respective "chip select" signal line, allowing for more sensors to be on the communication bus. The pressure sensors also have 5 oversampling ratio (OSR) levels to choose from, which dictate the sampling rate and resolution of the pressure sensor's ADC. The highest resolution RMS is 2.4 Pa, which typically takes 16.44 ms, and the lowest resolution RMS is 13 Pa, which typically takes 1.08 ms to sense. To achieve a 100 Hz loop rate, the middle OSR was chosen - a resolution of 5.4 Pa typically taking 4.16 ms.

The MCU selected was the Raspberry Pi RP2040, which is an ARM Cortex-M0+ running at 133 MHz [1]. This chip was selected because it has dual core functionality (to optimally allocate resources for control in future work), could communicate with I2C (for communication to the to other boards in future work) and SPI (for communication to the pressure sensors), was reasonably fast, as well as was available.

As shown in Figure 3.2, the PCB has 11 total footprints for pressure sensors, however, only 8 are populated. The three extra sensor footprints were laid out for the leading 4 pressure sensors if need to locate pressure sensors elsewhere due to wing structure interference, like a wing spar or other items. In current design the more central three footprints were not needed and the front 4 were just used.

3.3 Wind Tunnel Results

Multiple pairs of angle of attack and freestream velocity were retrieved successfully inside the wind tunnel. The initial tests were conducted with the freestream velocity ramped up, held at 13 m/s, then ramped back down.

The first case presented is a test case at 5° angle of attack. In Figure 3.3a, the estimates track relatively well when the wind tunnel is held at a high speed of 13 m/s. The velocity seemed to have a similar variance throughout the test; however, the angle of attack estimate has a variance that is clearly dependent on the freestream velocity. From the tests, it was noted that although the wind tunnel was turned off, the freestream velocity estimate was hovering around 3 m/s. This is due to the fact that at low velocities the noise of the sensors is larger than the nominal pressure drop.

The results also hold for angles of attack closer to stall. Figure 3.3b, shows the case when the wing section is set to 12° angle of attack. As in the previous case, the freestream velocity has a similar variance throughout the test and the angle of attack variance strongly correlates to freestream velocity. It should also be noted the angle of attack estimate strays from 12° when the freestream velocity is low.

3.3.1 Noise versus freestream velocity

Continuing to explore to the sensitivity calculations conducted in Chapter 2, the noise is compared for the angle of attack and freestream velocity estimates to the noise in simulations at the same conditions.

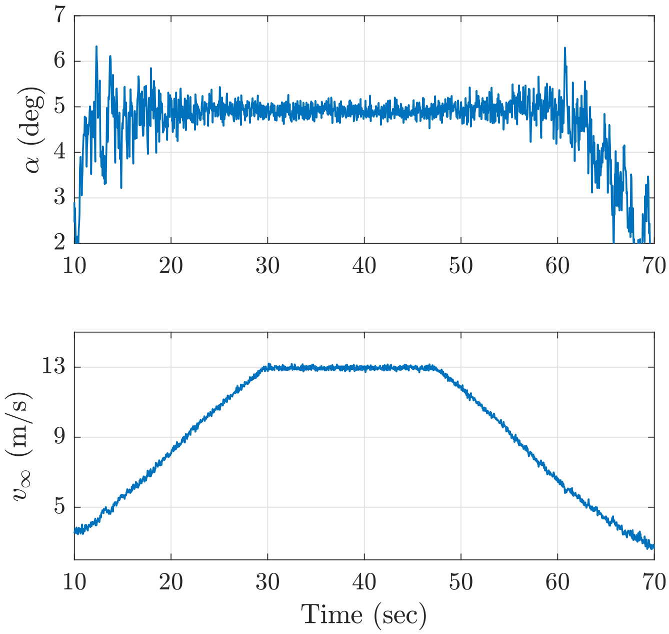

(a) $\alpha = 5°$

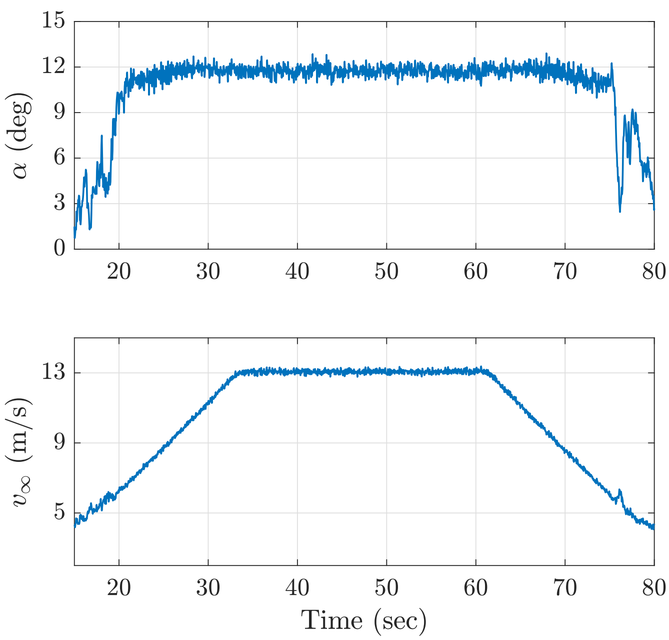

(b) $\alpha = 12°$

Figure 3.3: The output of the UKF for a NACA 2412 airfoil in the wind tunnel that was set at (a) 5° and (b) 12° angles of attack and had the airflow velocity sped up to 13 m/s then slowed back down.

The angle of attack estimate has a clear correlation with freestream velocity as seen in the ramp up, hold, and ramp down tests done. The relation was inspected with 5 different freestream velocities at 5° angle of attack. Figure 3.4 shows the standard deviation of the angle of attack estimate. The standard deviation of the angle of attack estimate from the wind tunnel tests was also compared with the standard deviation of simulations that were conducted over the same velocity range. The decrease in standard deviation of the estimate from the wind tunnel tests is consistent with that of the simulation results.

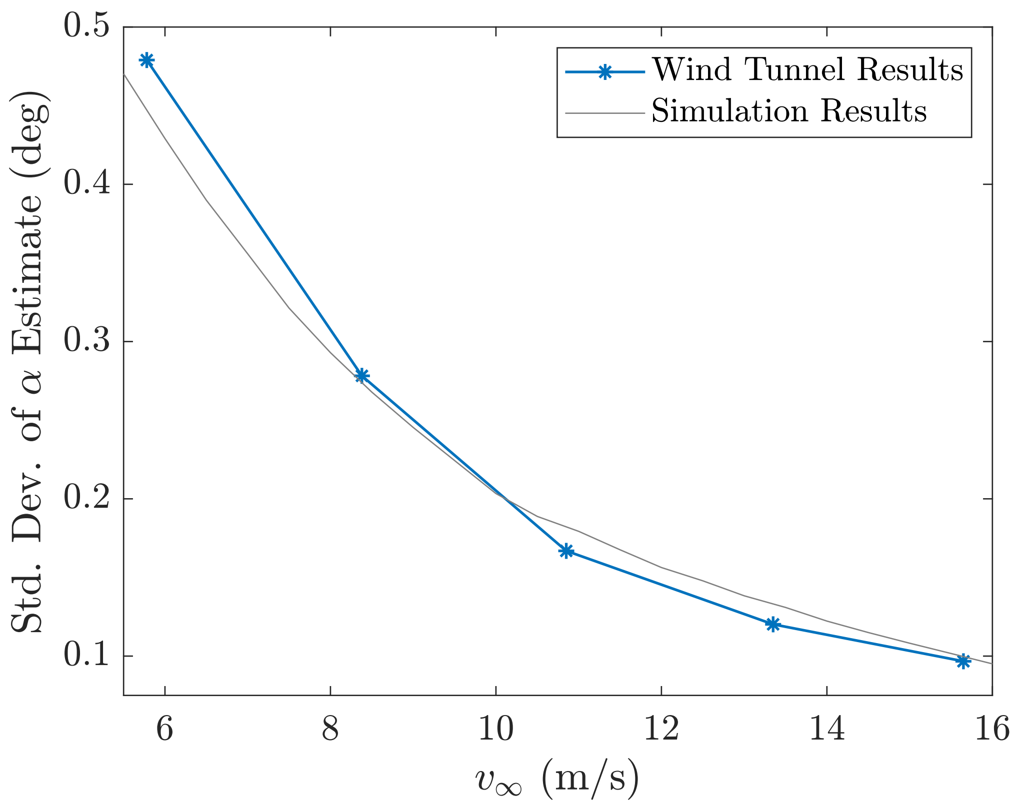

Figure 3.4: The standard deviation of angle of attack estimate with respect to freestream velocity when the NACA 2412 airfoil was at 5°. The wind tunnel tests were compared to simulation results.

Unlike for the angle of attack estimate, the freestream velocity estimate has a very small change in standard deviation with the change in freestream velocities that were tested. This can be seen in Figure 3.5, which was taken from the same 5 tests that were used to retrieve the angle of attack estimate noise. When compared to the standard deviation of the simulation results, the wind tunnel tests were reasonably close for the slowest 3 tests, however, the two fastest tests seem to have strayed from what the simulation predicted.

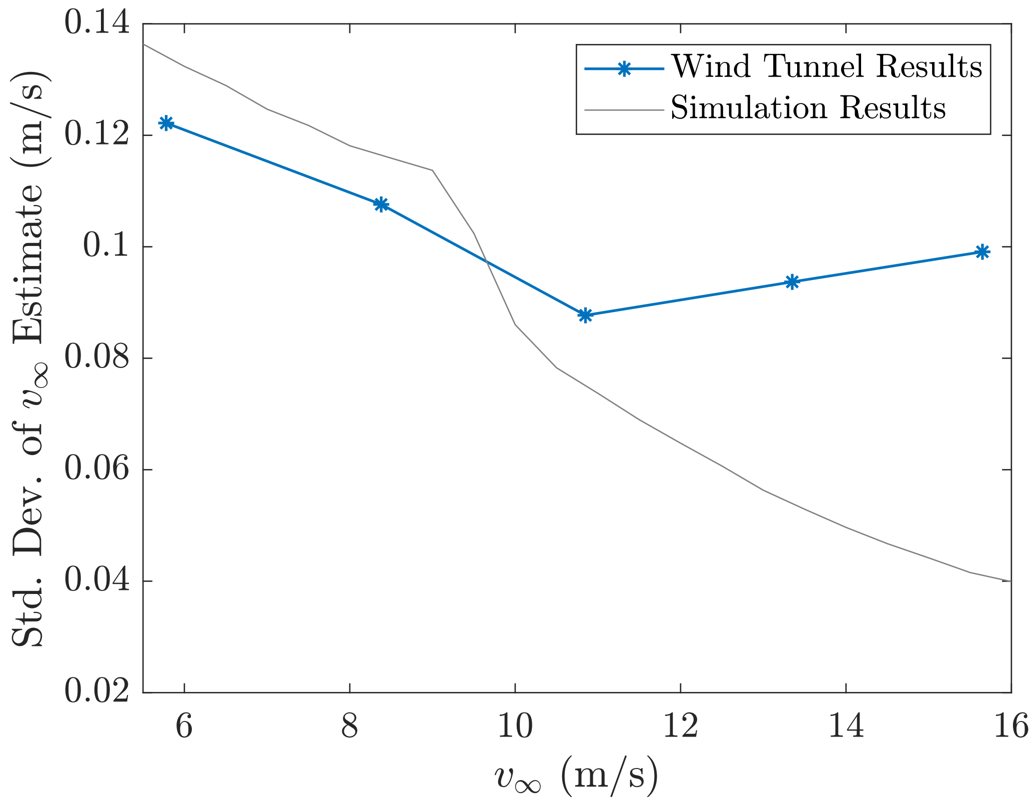

Figure 3.5: The standard deviation of freestream velocity estimate with respect to freestream velocity when the NACA 2412 airfoil was at 5°. The wind tunnel tests were compared to simulation results.

3.4 Concluding Remarks

It can be seen that the aerodynamic parameters can be retrieved from static pressure measurements on an airfoil using COTS pressure sensors. From the various tests, the angle of attack and freestream velocities were estimated accurately if the airflow velocity was sufficiently high enough. The variance also was dependent on the freestream velocity - the higher the velocity, the lower the variance was.

Just as in these tests results, traditional airspeed sensors have trouble detecting low speeds. In common manned airplanes, the airspeed does not “come alive” until the airplane has a measurable amount of airspeed in which the pressure system can differentiate the total pressure and the static pressure, measured by the pitot tubes, from their associated noise. On these common manned airplanes, the sensors are designed to be effective in the flight envelope of the airplane they are implemented on. Likewise, the pressure sensors on the chord can be fitted to the flight envelope that the airplane will be operated in. This could be done by choosing the appropriate fine-resolution, small-noise pressure sensors as well as varying the amount of pressure sensors used to estimate the aerodynamic pressure sensors. It should be noted from the work shown in Chapter 2, the closer the pressure sensors are located to the leading edge, the more efficient and effective the aerodynamic parameter estimate.

In future work, higher precision and accurate pressure can potentially be used to detect flow separation on the wind section to bound angle of attack estimates. This can help extend the effective flight envelope that the aerodynamic parameter estimation can be utilized without increasing the number of sensors.

Appendix

Here are results from the tests conducted in the wind tunnel for 5 different freestream velocities at 5° angle of attack to analyze noise in Figures 3.4 and 3.5. The scales were kept consistent so that they could easily be compared with one another. The tests were conducted at equally spaced frequencies of the wind tunnel's fan at 25 Hz, 35 Hz, 45 Hz, 55 Hz, and 65 Hz which translate to 5.78 m/s, 8.38 m/s, 10.85 m/s, 13.35 m/s, and 15.65 m/s, respectively. The dashed line represents what angle of attack the wing section was set using the markings on the wind tunnel mount or the freestream velocity that was measured using the VelociCalc anemometer for their respective plots.

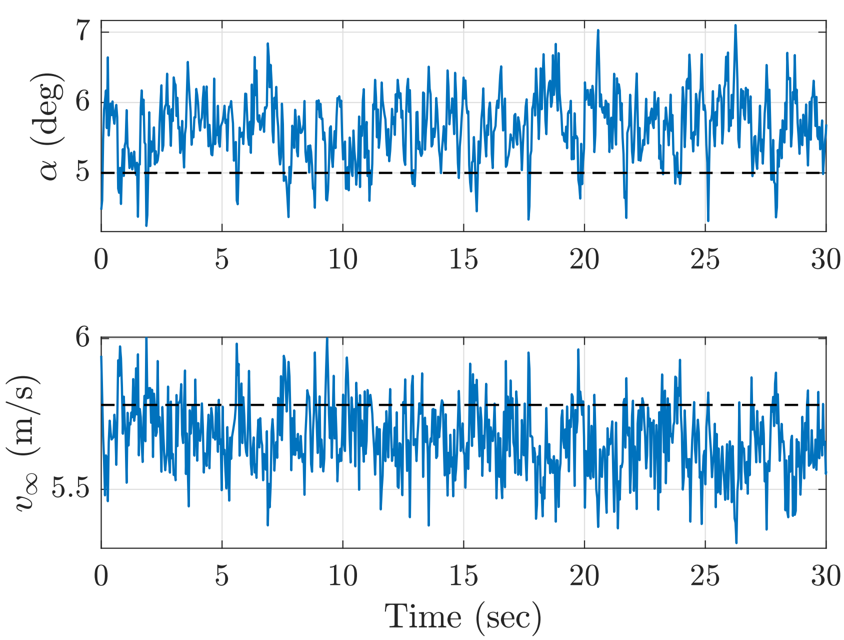

Figure 3.6: The estimates from the wind tunnel test conducted at 5° angle of attack and 5.78 m/s.

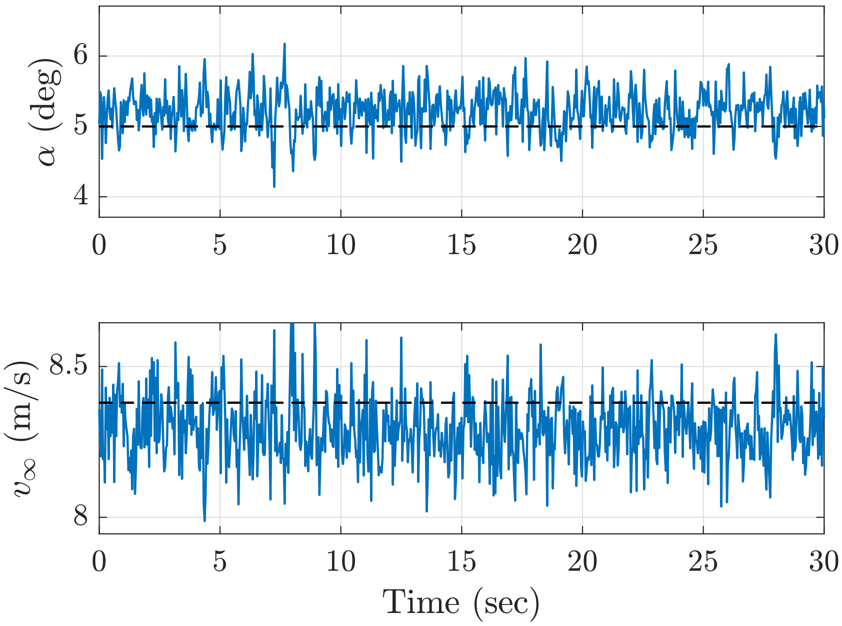

Figure 3.7: The estimates from the wind tunnel test conducted at 5° angle of attack and 8.38 m/s.

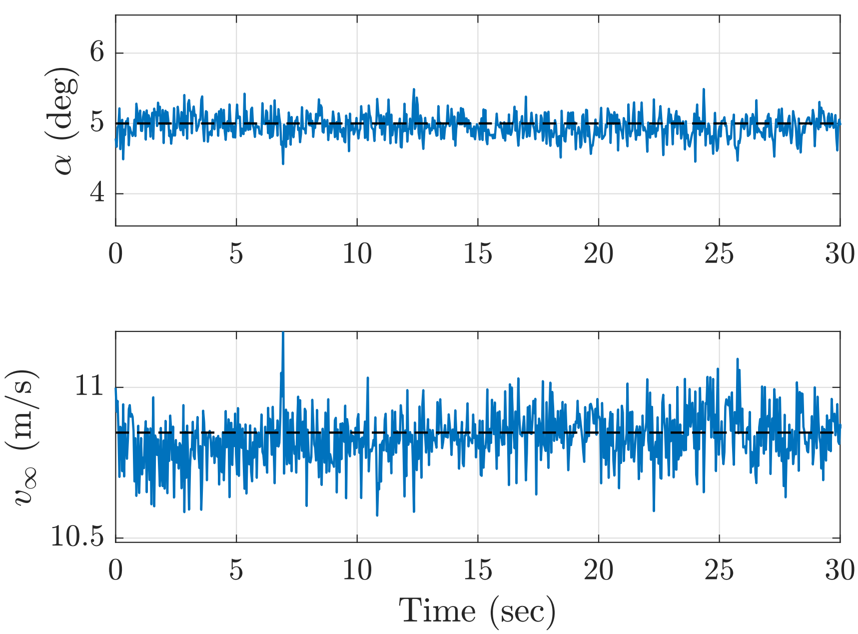

Figure 3.8: The estimates from the wind tunnel test conducted at 5° angle of attack and 10.85 m/s.

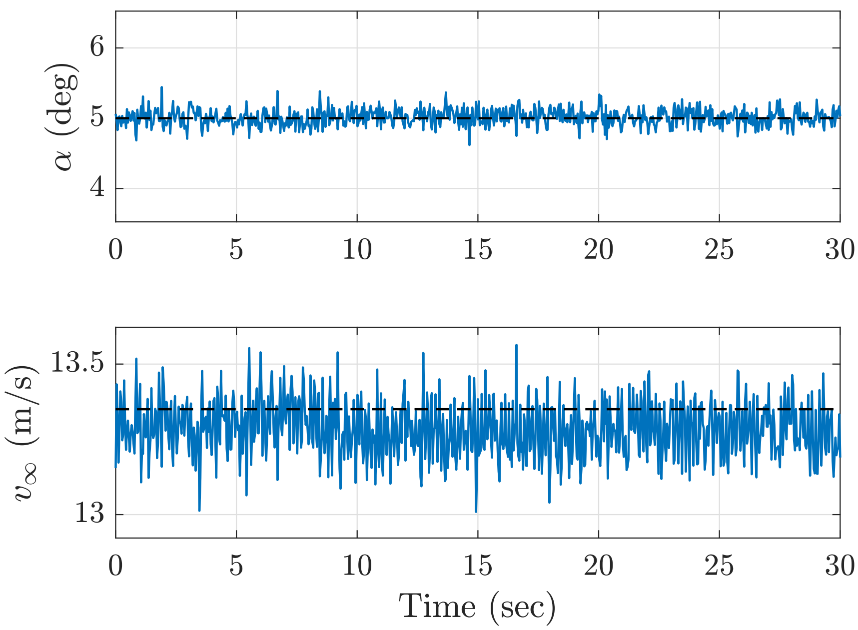

Figure 3.9: The estimates from the wind tunnel test conducted at 5° angle of attack and 13.35 m/s.

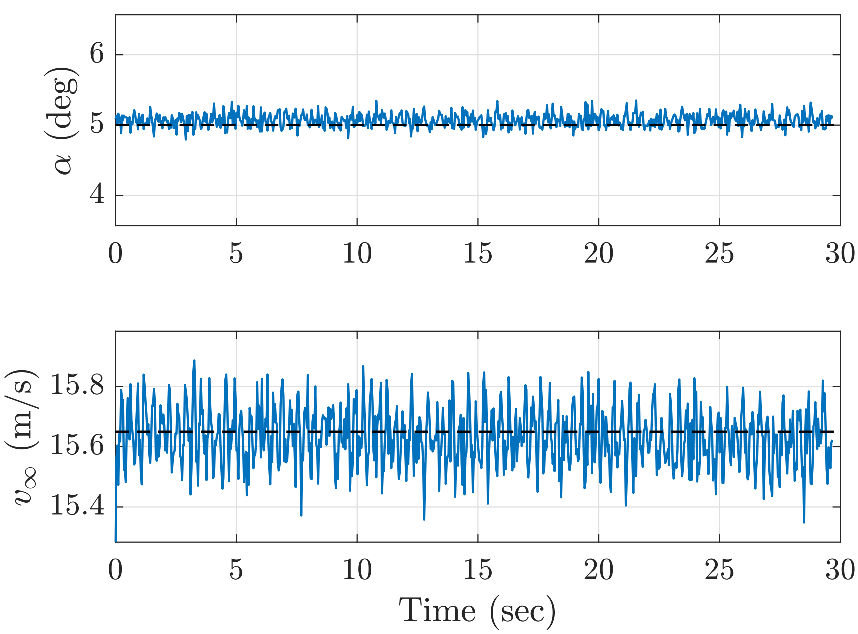

Figure 3.10: The estimates from the wind tunnel test conducted at 5° angle of attack and 15.65 m/s.

Chapter 4

Control Design utilizing Distributed Pressure Sensors with Roll Control Tests

Traditional autopilots use successive loop closure to control airplanes to achieve waypoints in 3 dimensional space [6]. A control diagram describing the loops is shown in Figure 4.1. The inner-most loop is an attitude controller that maneuvers the airplane into an attitude that the navigation controller desires. The attitude is estimated from a couple of attitude sensors, like IMUs.

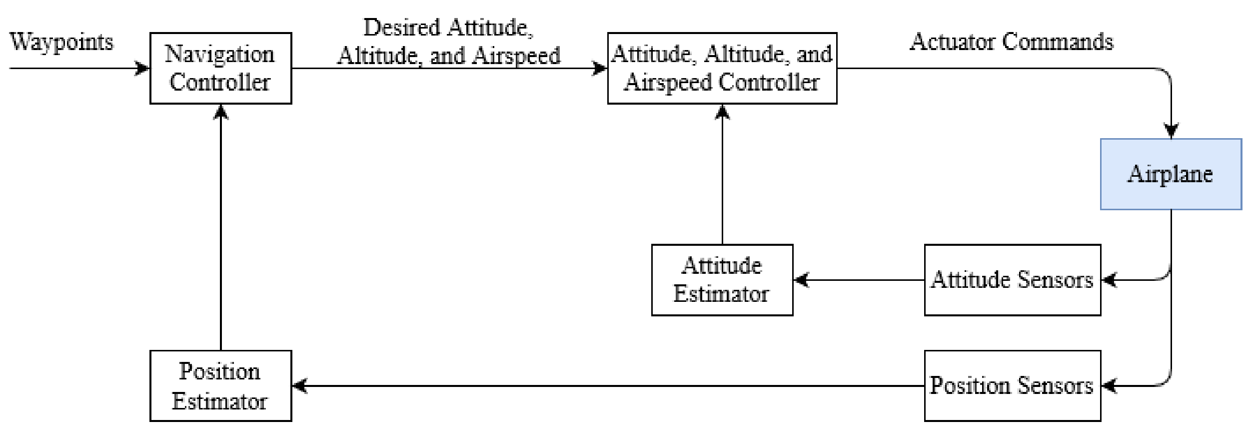

Figure 4.1: A traditional autopilot diagram that controls an airplane to follow a waypoint mission.

This method works well, but cannot detect localized disturbances and act accordingly. Localized disturbances can result in the controller requiring a input that cannot be fulfilled. This is because the airflow is at a different state when compared to a nominal state with the same sensor readings which were computed in CFD or in a wind tunnel. Traditional control derives PID gains from the stability gains from such nominal models.

In this chapter a new method of roll attitude control is introduced. Specifically, the method discretizes the wing into small sections and treats them as 2 dimensional airfoils. These sections are then integrated to estimate the resulting force and moment from the wing.

4.1 Control Scheme for Distributed Sensors

Distributed sensors over the aerodynamic surfaces can measure static pressure to help estimate the current state of airflow over the surfaces. These measurements can be used with various models for that estimation. However, many of these methods, like CFD, take long to compute and are not feasible for real time, closed loop control. Instead a method to discretize the wing into n more manageable sections is used as seen in Figure 4.2.

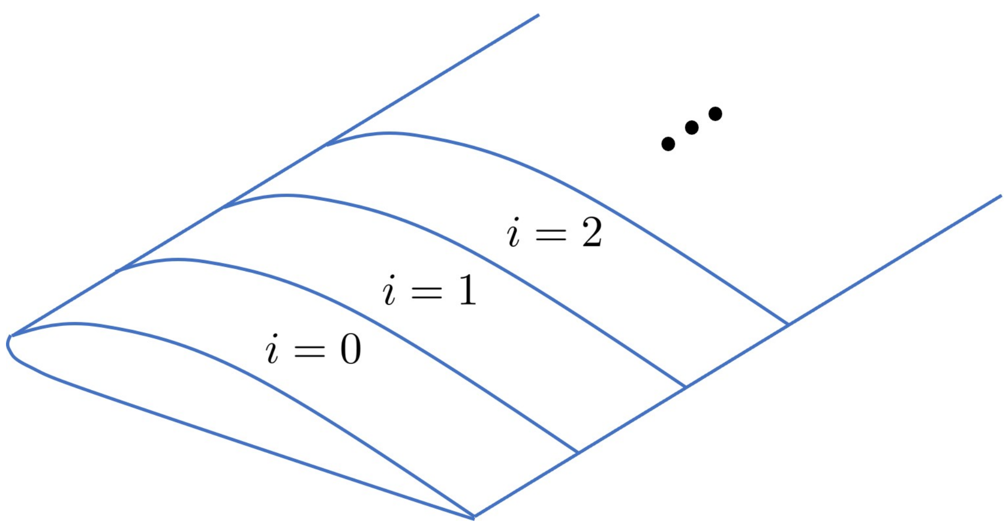

Figure 4.2: An illustration of a 3 dimensional wing sectioned up into small discretized wing sections.

Each section is looked at as a 2 dimensional airfoil. The pressure sensors associated with each section can be used to determine the aerodynamic parameters, angle of attack and freestream velocity for that section as investigated in Chapters 2 and 3. Estimation for the parameters using the UKF method is quick enough to retrieve the parameters to use in closed loop control. This analysis uses the assumption that spanwise flow of the wing is negligible.

When looking at the pressure profile of the entire wing, the lift force from the pressure differential between the top and bottom surfaces is lowest at the wing tips. This loss in lift is well known by aerodynamicists, and can be looked at as a lower effective angle of attack for the wing sections closer to the tips [4]. In this new control method, the sections at the tips, namely $i = 0$ and $i = n - 1$, will estimate a lower angle of attack when compared to the sections in between. An illustration of the discretized, nominal lift profile is seen in Figure

4.3; it shows how the outside sections will produce less lift. This profile would be different if a localized disturbance is applied - some sections can see a reduction or an increase in lift.

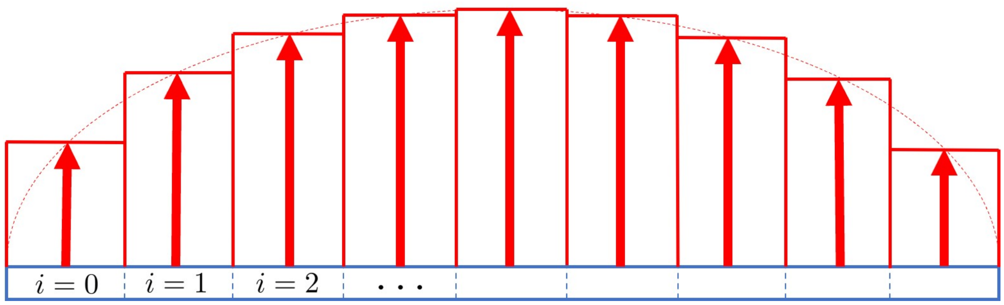

Figure 4.3: An illustration of a nominal lift distribution on a finite wing, with the discretized lift distribution estimates of each wing section.

To utilize the aerodynamic parameters of the discretized sections of wing, the traditional inside attitude control loop from Figure 4.1 was replaced with a modified attitude control loop shown in Figure 4.4. This modification still uses the attitude estimate to find the attitude error, however, it now sets the flaps based on a force and moment computation as well as an optimization problem with the new estimate of aerodynamic parameters derived from the distributed pressure sensors.

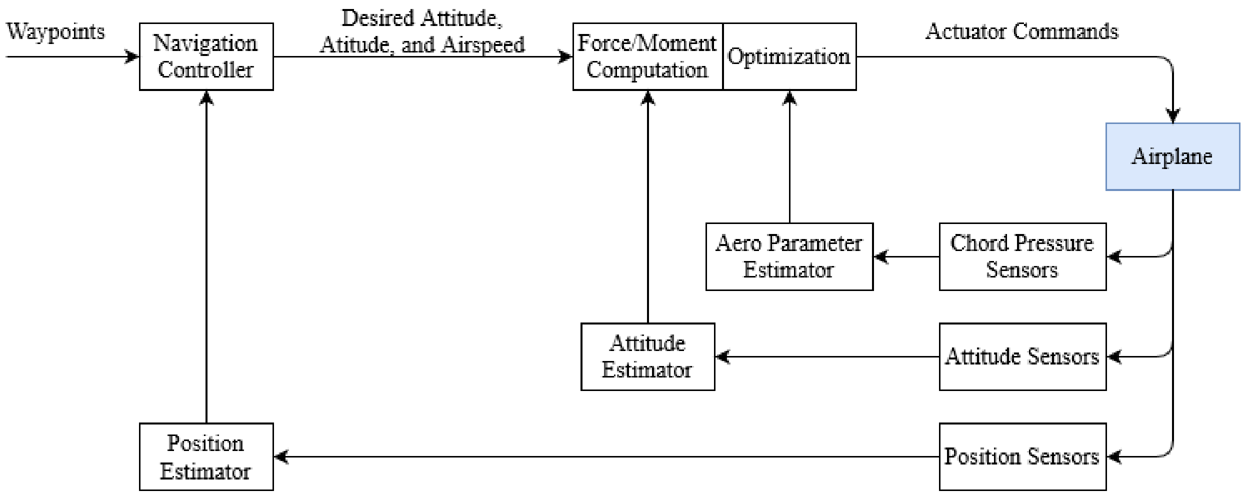

Figure 4.4: The modified control diagram of a plane. The inner loop has a novel attitude controller that uses airflow measurements from each wing section.

The force and moment computation is a straight forward 2nd order controller - to get from attitude errors to moments and forces. For this dissertation, this 2nd order controller was set to have a time constant of 0.1 seconds and be critically damped. The optimization problem uses the moment and force computations as constraints that the integration of lift, drag, and moment estimates must equate. Additionally, the flap deflection is constrained by the physical limits of the flap and the amount a flap can move in a single time step. The optimization then minimizes the drag of the entire wing by optimally deflecting flaps that achieve the proper forces and moments with the least amount of drag. This optimization can be changed to penalize other criteria, such as radar cross section that may be useful for stealth aircraft, but for this dissertation, drag was the only criteria being minimized.

To simplify the evaluation of the new controller, only the roll attitude was focused on, whereas the remaining states could still be controlled using a more traditional form of attitude control. The optimization problem to convert desired roll moment to all flap positions is described as:

$$\begin{aligned} \min_{\delta_i} \quad & \sum_i \frac{1}{2}\rho v_{\infty,i}^2 \cdot c_i \cdot dS_i \cdot C_{d,i}(\delta_i) \\ \text{s.t., } M_{\text{cmd}} &= \sum_i r_i \times \frac{1}{2}\rho v_{\infty,i}^2 \cdot c_i \cdot dS_i \cdot C_{l,i}(\delta_i), \\ \delta_i &\in \left[\delta_i^{\min}, \delta_i^{\max}\right], \end{aligned} \tag{4.1}$$

where ρ is the density of the air, $v_{\infty,i}$ is the estimate of the wing section's freestream velocity, c_i is the section's chord length, dS_i is the wing sections width, $C_{d,i}(\delta_i)$ is the wing section's coefficient of drag as a function of flap deflection, and $C_{l,i}(\delta_i)$ is the wing section's coefficient of lift as a function of flap deflection. $\delta_i^{\min}$ and $\delta_i^{\max}$ are the limits set on the flap deflection based on the the intersection of the flap physical limits and the limits the flap could move in a time step of the attitude control loop.

This optimization problem is required to solve quickly as it is part of the inner-most control loop described in Figure 4.4. The complete nonlinear model for $C_{l,i}(\delta_i)$ and $C_{d,i}(\delta_i)$ is not necessary and can be estimated with simpler expressions. A simple affine expression was used for the these functions, making the optimization problem a simple Linear Program. This allows for more discretized sections to be used without drastically slowing down the loop rate of the new attitude controller.

4.2 Experimental setup

The wing design used for the experiments of the new control method is comprised of 8 identical wing sections shown in Figure 4.5. These sections are 100 mm wide and have a chord length of 160 mm, with a 30 mm flap spanning the entire wing section. The same PCB design from Chapter 3 was used to measure static pressure at 8 points along the chord using TE's MS5607 pressure sensors and a 3.9 g RC servo to actuate the flap. The PCB and pressure sensors were centered for each wing section, but the RC servos were offset to the left, making each section have a small mass bias to the left. The section was made from extruded polystyrene with 3D printed inserts where the flap and spars interfaced the polystyrene wing section. The inserts were printed with ColorFabb's LW-PLA. The pressure ports were located at 5 *mm*, 10 *mm*, 15 *mm*, 20 *mm*, 73.8 *mm*, 86.3 *mm*, and 107.1 *mm* from the leading edge of the wing sections The pressure ports were printed on a Formlabs Form 2 SLA printer using Tough V4 resin. The ports were sealed to the pressure sensor on the PCB with silicone sealant.

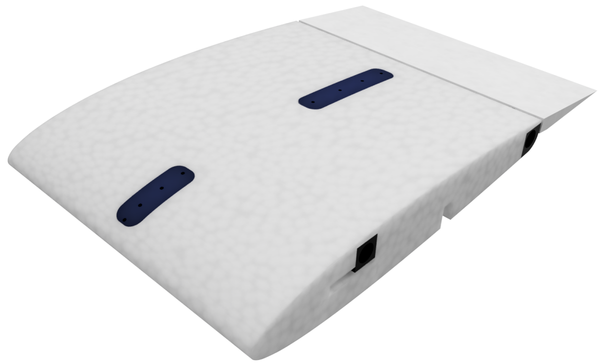

Figure 4.5: Rendered chord section of wing. Note: Pink extruded polystyrene was used instead of white expanded polystyrene.

The wing, shown in Figure 4.6, is comprised of 8 wing sections: 4 for each side of the wing. Along with a 75 *mm* fuselage width, the wing span resulted in being 875 *mm*. The sections are held together by two carbon rods that are the structural spars of the wing. The wing section PCBs are all connected via I2C to the main flight controller, a Navio2 by Emlid connected to a Raspberry Pi 4B. The flight controller ran a custom version of Ardupilot [37]. The software was written so that the control method could switch from a traditional control method to the newly proposed control method by user input. When the user chooses traditional roll control, the software runs a PD controller, where each side of

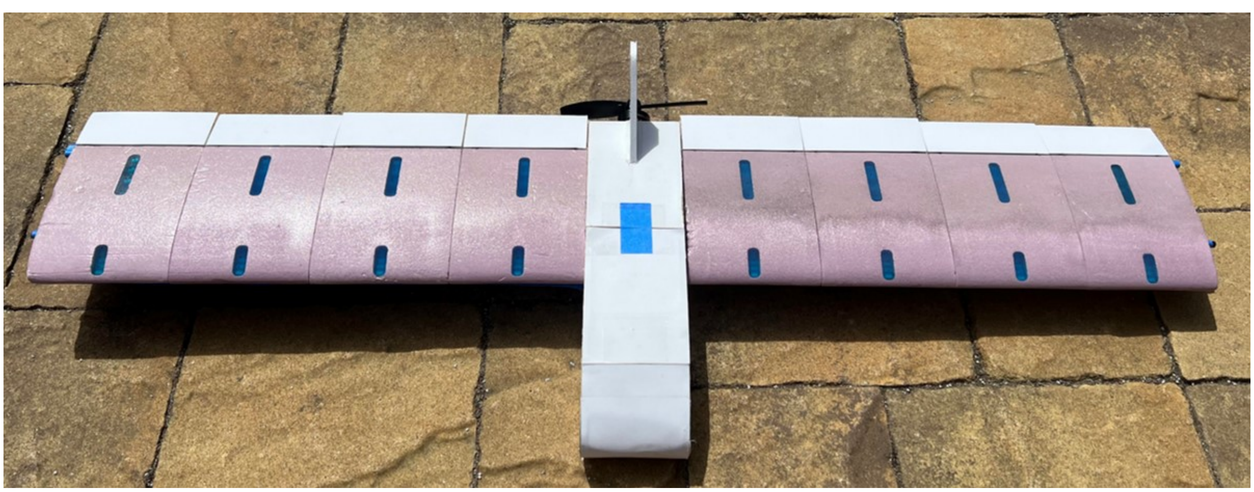

Figure 4.6: Picture of complete wing with 8 identical wing sections.

the wing section's flaps are commanded together acting as ailerons. When the user chooses the new control method, the flaps move to the positions commanded by the optimization problem's solution mention in the previous section.

There are two main setups for the experiments conducted on the wing. In the first setup, the wing was attached with a tether to a rotating boom. This boom was powered by a brushless motor that could swing the wing in a circle at approximately 4 rad/s. In the second setup, the wing was constrained to its roll axis with 2 bearings. It was then attached to the front of an electric bike. This second setup also had an option to have a movable flap controlled by the bike-rider mounted to locally disturb airflow. As the e-bike was ridden, air flowed over the wing and the flight controller controlled the wing to a desired roll angle. When there was no airflow over the wing, the wing leaned to the left (negative roll angle) due to the left-bias of mass from each section. This bias was minimal - when there was some airflow over the wing, both controllers were able to overcome that bias and level the wing. The bike was also ridden outside on a relatively flat street where external disturbances from the wind were present, although a best effort was made to conduct testing during less windy and less gusty days.

It should also be noted that the first setup on the boom was conducted indoors, and the second setup constraining all but the roll axis on the e-bike was performed after sunset. This is because TE's MS5607 pressure sensors are sensitive to sunlight. It was observed that pressure readings could swing on the order of kPa between being in direct sunlight versus being in the shade.

4.3 Experiments

Three sets of experiments were conducted to validate the new control algorithm. The tests were conducted to prove the measurement capability and accuracy on a multi-section wing, track a reference roll angle signal more efficiently and as accurately as a traditional controller, and be better suited at rejecting disturbances. Table 4.1, shows the three sets of experiments conducted along with their objectives. Figure 4.7 shows diagrams of the the wing test setups.

Test	Objective
Circle "Lasso" Test	Retrieve freestream velocity gradient along wing
Step Reference Response	Track reference roll angle with better efficiency
Step Disturbance Response	Better disturbance rejection

Table 4.1: Table of experiments conducted with each experiment's objective.

4.3.1 Circle "Lasso" Tests

This first test, the Circle "Lasso" test, was conducted as a proof of concept to show that the wing could accurately measure variable airflow across the wing. Using the rotating boom

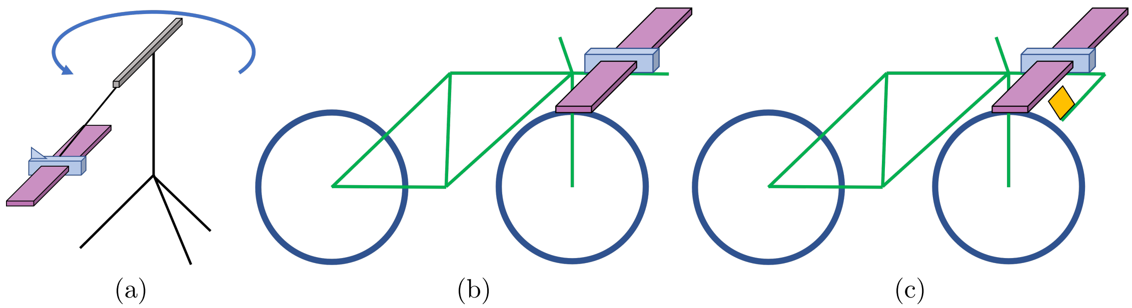

Figure 4.7: These are diagrams of the tests conducted. (a) The motorized boom setup for the Circle "Lasso" test. (b) The setup of the wing using two bearing on an e-bike for the step reference response test. (c) The setup of the wing using two bearing on an e-bike with a flap to cause a localized airflow disturbance for the step disturbance response test.

setup (Figure 4.7a), the wing was swung in a circle at around 4 rad/s. The center of the wing, the fuselage, was located 1 m from the center of rotation. During this test, the freestream velocity was estimated by each wing section. The computed radius was then derived from the freestream velocity estimate divided by the yaw rate of the wing as shown by:

$$R_{\text{computed}} = \frac{v_\infty}{r} \tag{4.2}$$

where v_∞ is the estimated freestream velocity of the current wing section and r is the yaw rate of the wing. The results are shown in Figure 4.8.

Note that the rotation speed was not exactly constant during this test due to the periodic nature of the setup. Therefore, rather than looking at the estimated freestream velocity at each section, as it varied with the rotation speed, the measured radius was compared to the computed radius to determine the accuracy of the estimates.

For a perfect estimate, without errors or noise present, the calculated radius should be the same as the measured radius. The dashed line in Figure 4.8 represents this ideal scenario. It should also be noted that the outside sections of the wing would see a higher freestream velocity while the inside sections would see a lower freestream velocity. For the wing sections that were further from the center of rotation, the calculated radius, and therefore freestream velocity estimate, accurately predict the measured radii as shown in Figure 4.8. However, this trend does not hold true for the wing sections closer to the center of rotation. The calculated radii and estimates are higher than expected. This is due to the freestream velocity estimate not being accurate at lower velocities. As seen in Chapter 3, at lower airflow velocities, due to pressure sensor noise, the estimates incorrectly output velocity values larger than the true velocity. Hence, the results successfully illustrate differences in localized airflow, given sufficient airflow velocity.

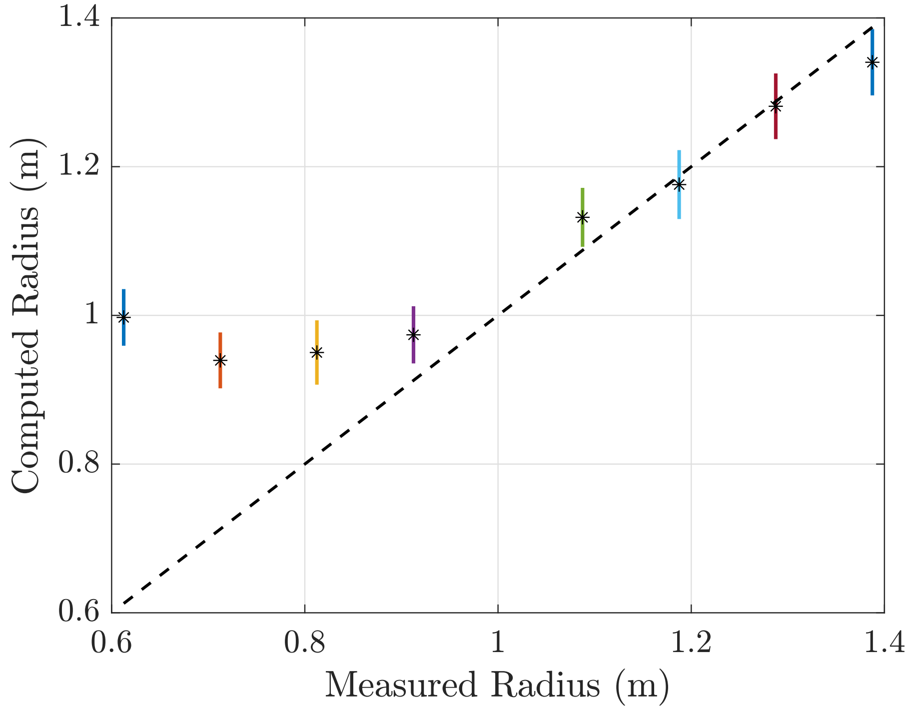

Figure 4.8: Results from the Circle “Lasso” test show how the various wing sections’ estimates of the freestream velocity divided by the yaw rate of the wing can reproduce the measured distance of each wing section to the middle of rotation. A perfect estimate would result in data points being on the dashed line.

4.3.2 Step Reference Response Tests

The step reference response test was conducted using the e-bike setup (Figure 4.7b) with the goal of tracking a reference roll angle with improved efficiency. In this test, the reference roll angle was a square wave with a period of 6 seconds and an amplitude of 10°. The approximate time of each test was just under 15 seconds, or about 2 periods of the reference roll signal.

First, a baseline test was conducted using a traditional roll controller, which consists of a PD controller that uses an IMU. The results of the reference tracking of this controller can be seen in Figure 4.9a. As described in the experiment setup, at the beginning of the test, the wing started with a lean to the left (a negative roll angle) due to a left-mass bias. When airflow began flowing over the wing, the flaps gained sufficient control authority to follow the reference square wave roll angle. This test demonstrated that the traditional roll controller was able to track the reference signal.

The next test was conducted using the new roll controller which utilized the velocity and angle of attack estimates. The results of the reference tracking of this controller can be seen in Figure 4.9b. Again, it is apparent that the controller was able to track the square wave

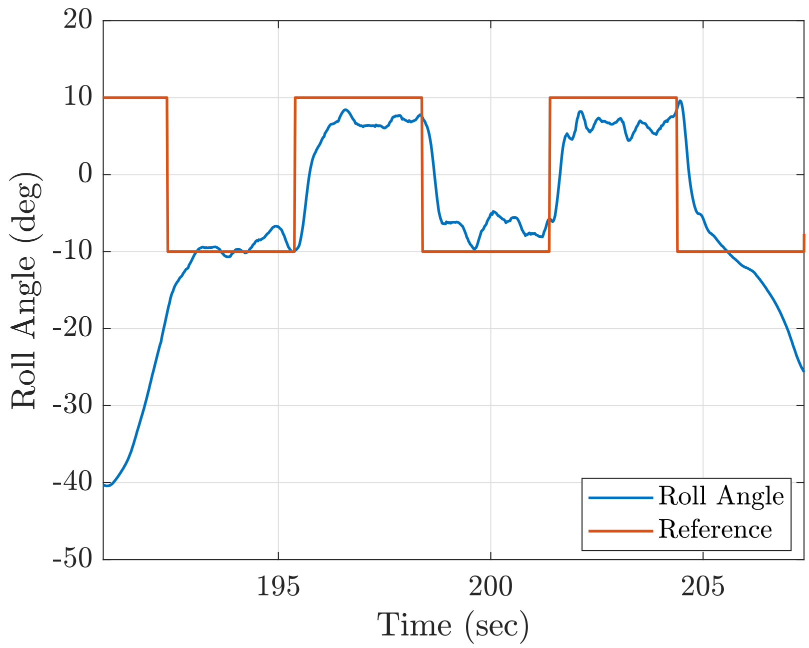

(a)

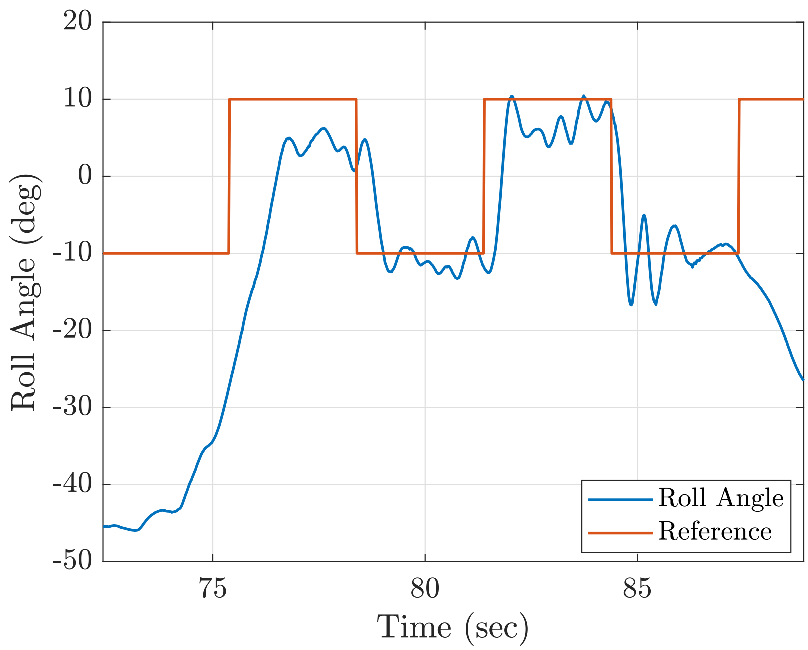

(b)

Figure 4.9: Step reference response of roll attitude using (a) a traditional roll controller and (b) the new roll controller.

reference signal.

During both tests, the angle of attack and freestream velocity estimates were recorded - the traditional roll controller did not, however, utilize these measurements. These estimates were used to compare efficiency between both controllers. Due to the nature of these tests being conducted on a bike where the exact same velocity profile was not achievable, an estimated coefficient of drag for the entire wing was compared. This coefficient of drag was averaged on two steps and the two roll control methods were compared. The results shown in Figure 4.10, show that the new control method is nominally more efficient. However, it is also seen that shortly after the step, the new control method is not more efficient for less than 0.5 *sec*.

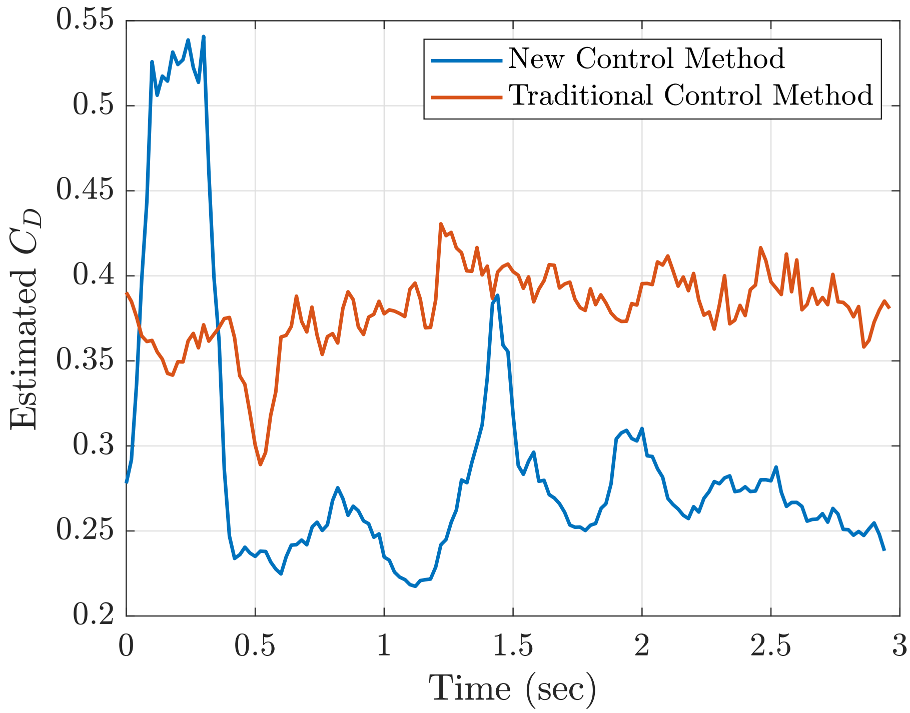

Figure 4.10: A comparison of the averaged estimated coefficient of drag for two reference steps.

4.3.3 Step Disturbance Response Tests

The step disturbance response test was conducted using the e-bike setup (Figure 4.7c) to demonstrate localized disturbance rejection. In this test the reference roll angle was set to 0°. When at speed and the wing was about level, a flap was deflected to disturb the airflow on the right side of the wing. The approximate time of each test was about 15 seconds.

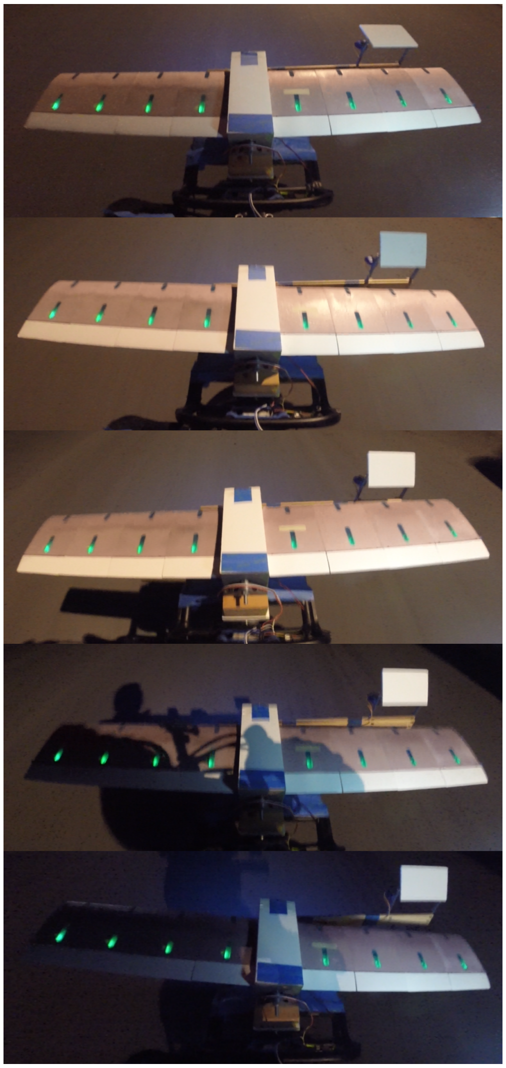

(a) Traditional Control Method

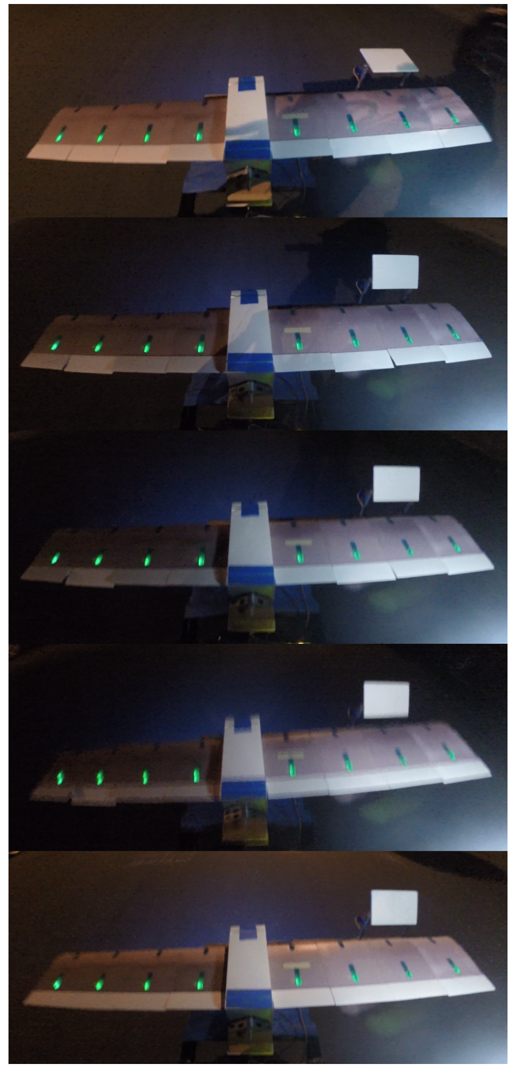

(b) New Control Method

Figure 4.11: Pictures taken during the disturbance test spaced 1 second apart. The flap is deployed shortly after the first image, causing a localized airflow disturbance on the right-most sections. (a) Shows the results of a traditional controller. (b) Shows the results of the new controller - note the independent flap segment responses on right wing.

First, looking at a traditional controller, the localized airflow disturbance will not be measured but its effects on the roll attitude will still try to be rejected by the controller. The results of the traditional controller can be seen in the stills in Figure 4.11a and the plot in Figure 4.12. By the last frame in the stills, the wing is tilted considerably more to the right. Analyzing the plot, the localized airflow step disturbance occurs just after the 200 seconds mark, and the wing first dips closer to the 0° reference angle then dips to the right as a result. It is important to note that testing over multiple runs the wing attempts to return to level, but always has a larger steady state error due to the airflow disturbance. The controller does not know about the disturbance and was still trying to control the plane as if there were no disturbance. The steady state error can be minimized with larger gains, but that comes at a cost of a more jittery controller during nominal airflow conditions.

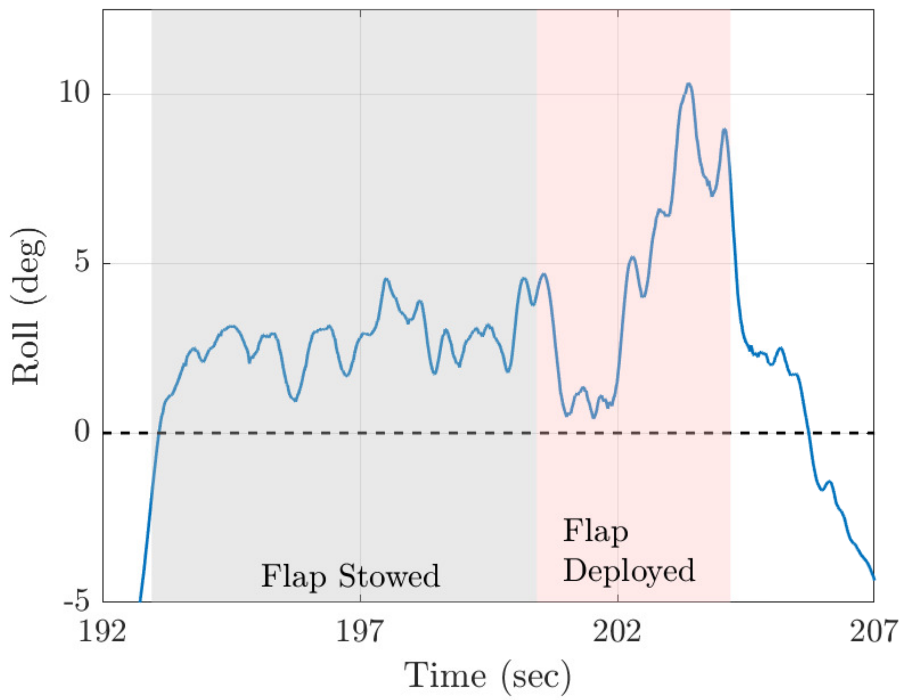

Figure 4.12: The roll attitude response from step disturbance test using a traditional controller. The localized disturbance was imparted on the right-most section of the wing at just after 200 seconds.

Next, the new controller was tested with the localized airflow disturbance. This time the centralized controller got the additional information about the disturbance through the change in angle of attack estimates on the wing sections. The results of the new controller can be seen in the stills in Figure 4.11b and the plot in Figure 4.13a. The time when the disturbance is imparted on the wing is less noticeable than the test with the traditional controller when just looking at the roll angle of the wing. However, from the pictures taken during the test, it can be seen that each section's actuators are moving independently of each other to reject the disturbance. The roll angle stays consistent throughout the test, proving that the disturbance was rejected better.

The step disturbance is also well visible in the angle of attack estimates. These estimates of angle of attack are shown in Figure 4.13b. Before the flap was deployed (localized step disturbance), the right-most wing section, $i = 7$, is measuring a lower angle of attack when

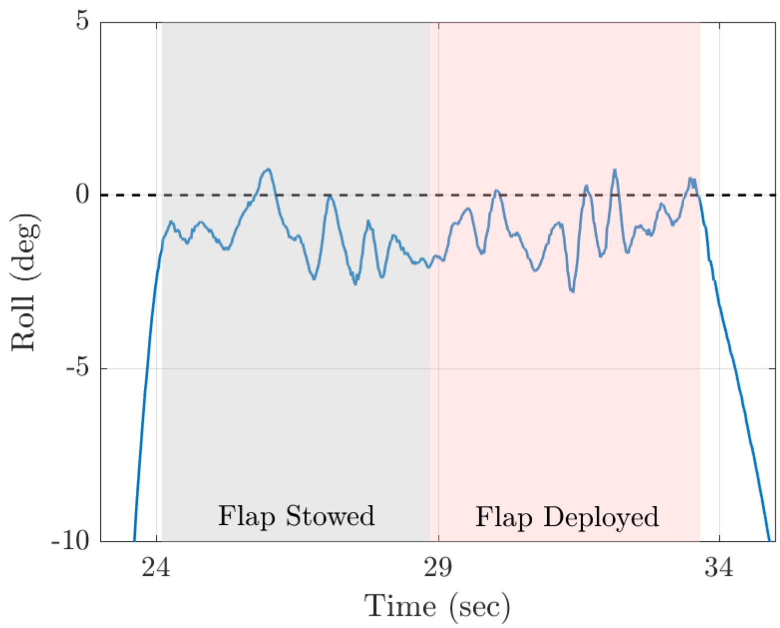

(a)

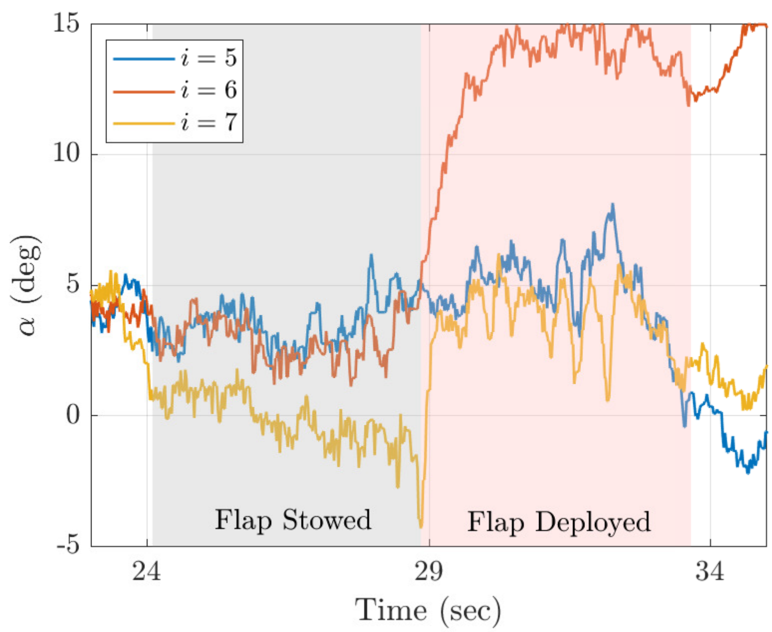

(b)

Figure 4.13: (a) The roll attitude response from step disturbance test using the new controller. (b) The estimate of angle of attack of the three right-most wing sections during the same time. The localized disturbance was observed and measured by the two right-most sections of the wing at just before 29 seconds, but not for the 3rd right-most section, $i = 5$.

compared to the sections next to it, $i = 5$ and $i = 6$, although the sections are rigidly mounted to each other with no wing twist. These angle of attack estimates follow the theory that the high pressure on the bottom of the wing bleeding over the wingtip to the low pressure region on top of the wing is consistent with a lower effective angle of attack. [4] However, the estimates drastically differ when the flap, localized disturbance, is deployed. It is observed that the disturbance specifically changes the airflow to not only the right-most section, $i = 7$, but also the section next to it, $i = 6$. Both estimates measure an increase in angle of attack as the flap is deployed, whereas the $i = 5$ section remains unchanged. This information was able to be utilized by the central flight controller to set the flap positions accordingly resulting in significantly better roll angle tracking.

4.4 Concluding Remarks

The use of distributed pressure sensors in a control loop was shown in this chapter. A wing was discretized into sections, where each section was analyzed separately. Each section measured pressure sensors to retrieve an estimate of the airflow. An experiment conducted showed that localized airflow was retrieved accurately if at sufficiently high freestream velocities.

A centralized flight controller could then use the estimates in a control loop to solve a minimization problem to determine the optimal flap deployment for desired attitude. The new control method introduced was shown to be a viable replacement for traditional controls on a 0.875 m wing through two experiments. The controller was successfully demonstrated on both following a reference signal and rejecting a localized airflow disturbance. During the reference signal tracking test, it was also shown that the cost metric that was decided on to be minimized in the optimization block of the controller, drag, was lower than that of the traditional controller.

Chapter 5

A Tactile Sensor for Distributed Pressure Sensing on Fixed Wing Flyer

A wide variety of robotic tactile sensors have been developed using transduction techniques such as capacitive, optical, and resistive [16]. While tactile sensors typically measure contact forces in grasping, highly sensitive arrays can be used for measuring pressure distributions resulting from airflow around surfaces. In addition to high sensitivity for airfoil applications, it is also required that the sensors be low profile, conformal to a surface, and easily able to cover a wide area. Considering the availability of integrated electronics for capacitive touch screens (e.g. [15]), capacitive tactile sensing is an attractive choice. Table 5.1 shows representative capacitive tactile sensors, starting with the pioneering array sensor of Boie [7]. As shown in [7], capacitive sensors have low noise, giving sensitivity limited largely by the cell nominal capacitance and compliance. In the table, time/cell indicates the rate at which a cell updates its measurements, where by averaging 100 measurements, the resolution can be improved by a factor of 10. In this chapter, a tactile sensor array that measures pressure distributions across aerodynamic surfaces is introduced and optimized. This sensor is indicated on the last two rows of Table 5.1.

Array Size	Cell Size	Resolution	Time/Cell	Reference
8×8	$2.5 \times 2.5\ mm^2$	?	$40\ us$	[7]
8×8	$3.3 \times 3.5\ mm^2$	$600\ Pa$	$2.2\ ms$	[11]
8×8	$0.1 \times 0.1\ mm^2$	$2.3\ kPa$	$80\ us$	[14]
5×5	$1 \times 1\ cm^2$	$2.5\ Pa$	$10\ sec$	[27]
1×10	$\approx 1\ cm^2$	$60\ Pa$	$1\ ms$	[15]
1×22	$7 \times 8\ mm^2$	$100\ Pa$	$1.9\ ms$	[28]
10×15	$1 \times 1\ cm^2$	$25\ Pa$	$1\ ms$	Preliminary Design
10×15	$1.5 \times 1.5\ cm^2$	$20\ Pa$	$1\ ms$	Optimized Design

Table 5.1: Representative capacitive tactile sensors

The sensor array designs introduced in this chapter falls within the range of resolution and update rate of the cells of comparable size shown in Table 5.1. To demonstrate the pressure distribution measurements during flight, the preliminary array design was installed onto the wing of an RC airplane and tested at speeds up to 12 m/s. The results are then compared to results of the same airfoil generated through a 2D airflow analysis using XFOIL [10].

5.1 Preliminary Sensor Design

The preliminary sensor array being presented in this chapter utilizes capacitance measurements to determine pressure distributions. An increase or decrease in pressure moves the two electrodes closer or further apart, resulting in increased or decreased capacitance, respectively. For these types of pressure sensors to be applicable on airplanes, they must be able to map static pressure distributions across a wing or aerodynamic surface.

5.1.1 Dielectric Material Spring

If two similarly sized electrodes are kept parallel to one another, the capacitance is inversely proportional to the distance given by:

$$C = \epsilon_0 \frac{A}{\delta} \tag{5.1}$$

where ϵ_0 is the dielectric constant, A is the area of one of the electrodes, and δ is the distance between the electrodes.

A dielectric material insulator can be placed between the electrodes, acting as a spring, to relate pressure on the electrodes to capacitance. Assuming the change in dielectric constant from the insulator being squeezed is negligible, the pressure to capacitance equation is:

$$\Delta p = E\left(\frac{\delta_1 - \delta_2}{\delta_1}\right) = E\left(1 - \frac{C_1}{C_2}\right) \tag{5.2}$$

where Δp is the pressure change and E is the Young's modulus of the insulator. Rewriting the resulting capacitance from the applied pressure change as $C_2 = C_1 + \Delta C$, then with small ΔC, (5.2) can be estimated as:

$$\frac{\Delta C}{C_1} \approx \frac{1}{E}\Delta p \tag{5.3}$$

This shows that the ratio between the pressure change and percent capacitance change is approximately the inverse of the Young's Modulus of the insulator. Therefore, the sensitivity of this design is dependent on the Young's modulus: less stiff dielectric material results in a greater capacitance percent change for a unit pressure change. However, obtaining low modulus dielectric materials (e.g. $\approx 10kPa$) with low hysteresis can require microstructured materials [32], and the 10 kPa dielectric would give only a 1% change at the nominal aerodynamic load of 100 Pa.

5.1.2 Clamped Beam Spring

To create a higher sensitivity pressure sensor, the electrodes must have a larger change in distance for the same pressure change. This can be achieved if the elastic dielectric layer is swapped for a suspension design where the electrode is only supported at the edges, as seen in Figure 5.1. In this pressure sensor, the suspension design has supports on all four sides. The membrane is modeled as a two-dimensional beam so that an analytical model can be utilized. This 2D model is a fixed-fixed beam with uniform load, where the pressure to displacement relation is:

$$\Delta\delta(x) = -\frac{x^2}{2t^3E}(L-x)^2\Delta p \tag{5.4}$$

where E is the Young's modulus of the top conductor, t is the thickness of the membrane, L is the distance between the membrane supports, and x is the distance from one of the supports. Note that using this type of model will overestimate the displacement as the conductor near the unmodeled fixed edges will displace less than what the model predicts.

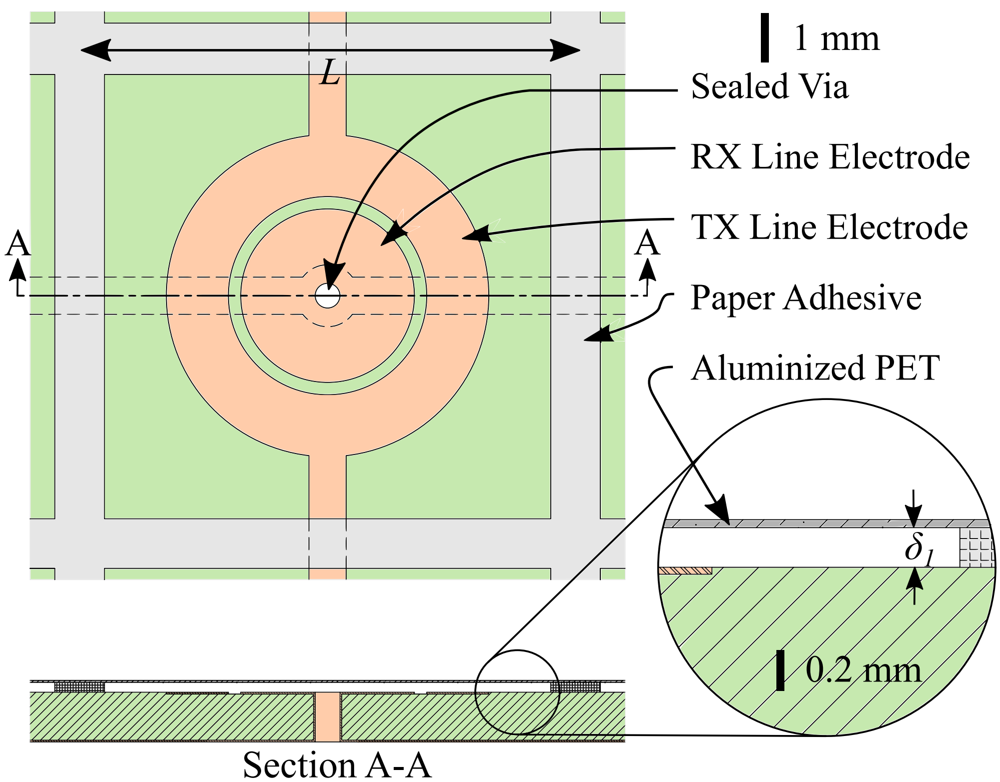

Figure 5.1: The model of a single capacitive cell in the sensor array. Each cell's area is 1 cm^2. The paper adhesive is comprised of thermal adhesive on both sides of paper. The aluminized polyester has the aluminium face down and has been removed in the top view to show more detail. Additionally, a ground-fill (not pictured) was used on both layers where there were no electrodes to shield the cell from electrical noise.

The relationship between the change in pressure and the change in capacitance is derived in [14]:

$$\frac{\Delta C}{C_1} \approx \frac{L^4}{60t^3\delta_1 E}\Delta p \tag{5.5}$$

where δ_1 is the original distance of the gap before a pressure is applied. This equation shows that if $\frac{L^4}{60t^3\delta}$ is greater than 1, then the suspended membrane design will see a larger percentage change in capacitance for the same pressure change when compared to the design using the dielectric material insulator as a spring.

The material of the top conductor is aluminum coated polyethylene terephthalate (PET) film with thickness t, of 40 μm and has a Young's modulus, E, of approximately 3.0 GPa [25]. Using paper with thermal adhesive on both side for the supports of the membrane results in an original distance, δ_1, of 0.2 mm. With the same nominal aerodynamic loading, as Section 5.1.1, of 100 Pa, a 43.4% change in capacitance would be expected for a double clamped beam, with significantly lower sensitivity for the membrane clamped at 4 edges.

The sensor was, therefore, chosen to be 1 $cm \times 1$ cm with a suspended membrane design. However, rather than having one electrode fixed and one electrode on the membrane, both electrodes were fixed and a grounded aluminized polyester film membrane was used. The electrodes were designed to be a low cost 2-layer PCB as seen in Figure 5.1, while the grounded membrane provides some electrical noise shielding. The sensor was fabricated by laminating laser cut adhesive film to the FR4 PCB, followed by laminating the aluminized polyester layer.

5.1.3 Capacitance Array

Capacitive sensors are readily arrayed. A set of sensors in an array can share an electrode, where the only requirement is that the other electrode is not shared between any of the sensors in that set. To efficiently array these sensors, two sets of electrodes can be arranged perpendicularly in lines ensuring no two electrodes in the same set form a capacitive sensor. In Figure 5.2, one set of electrodes is configured vertically while the other set is configured horizontally.

The capacitive pressure sensor array uses the IQS550 capacitive trackpad IC from Azoteq to measure the capacitance of the sensors. This IC has 15 transmit lines and 10 receive lines. Each transmit line can be sensed by each of the receive lines, therefore, the largest array one IQS550 IC can support is 150 cells. The IC measures the capacitance and outputs values that are relayed via an I2C bus. Using the sensor design in Figure 5.1, the IC can reliably read all 150 cells and convey the information through the bus every 150 ms.

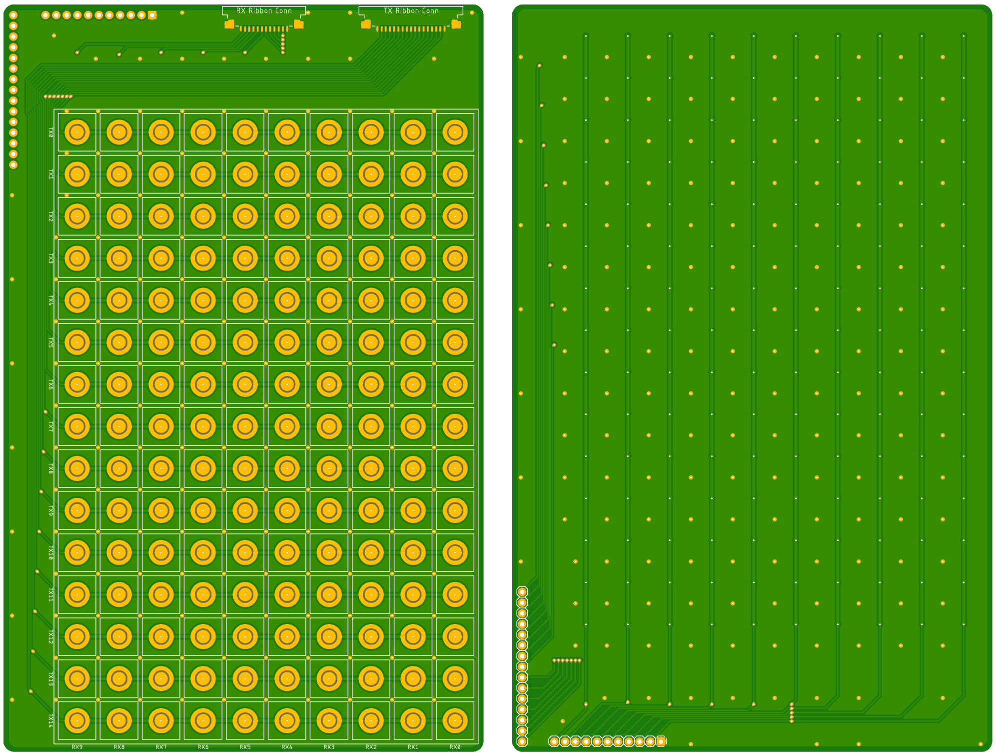

(a) (b)

Figure 5.2: The prototype rigid PCB design of the pressure sensor array. (a) Shows the top of the board. (b) Shows the bottom of the board. In both figures, the left side is closest to the leading edge when mounted on the wing for the tests.

5.2 Capacitive Pressure Sensor Tests of the Preliminary Design

To test the capacitive sensor array, the rigid PCB shown in Figure 5.2 was mounted flush on the top surface of a wing with a span of 1.1 m, chord of 20 cm, and thickness of 1.3 cm.

The PCB was recessed into the wing to ensure that the airflow was not disturbed during testing. The array was also placed away from the wingtips to minimize the effects of wingtip vortices. The mainly flat airfoil is pictured in Figure 5.3. The first row of elements in the sensor array are located 2 cm from the leading edge and the last row of elements are located just before the airfoil begins to taper off. The receive lines for the Azoteq IC start with RX: 9 closest to the leading edge and end with RX: 0 closest to the trailing edge. The transmit lines for the Azoteq IC start with TX: 0 closest to the wing root and end with TX: 14 closest to the wing tips.

Alternatively, a flexible PCB could be similarly applied to the surface. In this case, a recess to prevent the flexible PCB from disturbing the airflow would not be necessary. The

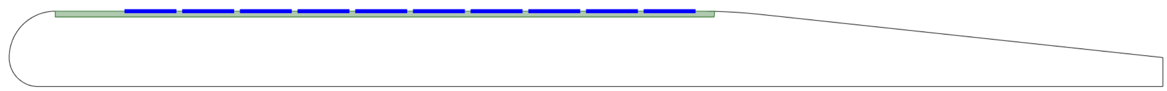

Figure 5.3: The airfoil used to confirm the preliminary capacitive pressure sensor array on the RC airplane. The blue highlights show the locations of the individual pressure sensor array cells on the airfoil. The airfoil's chord is 20 cm.

use of a flexible PCB could also be beneficial when mounting the sensor array as it would allow a non-flat surface to be used. For example, the array could be used on a common NACA airfoil rather than the flat airfoil presented in this paper.

Testing of this pressure sensor array was performed on a wing mounted on a test fixture protruding from the back of a pickup truck. The sensor array collected pressure measurements while the truck was accelerated from 0 m/s to approximately 12 m/s, then decelerated back down to 0 m/s. A wind vane was located below the wing to ensure that the airflow was undisturbed by the body of the truck. In addition to collecting pressure measurements from the sensor array, an LPS25H STMicroelectronics barometer logged ambient air pressure and a Wind Sensor Rev C Modern Devices anemometer logged freestream velocity. While the tests were aimed to be conducted in a still air, no wind environment, light breezes were inevitable.

5.2.1 Calibration

The pressure sensor array was calibrated to account for manufacturing and temperature deviations. To ensure accuracy, the pressure sensor array was calibrated on the wing rather than off of the wing in a pressure chamber. This is due to the fact that the extruded polystyrene wing touches the PCB and therefore adds stray capacitance, making calibration of the array off of the wing in a pressure chamber inaccurate.

The calibration process assumes that the relation is linear, as approximated in (5.5). Since the test location was situated on a slightly inclined road, measurements at the top and bottom of the road were taken on both the capacitive pressure sensor array and the barometer. The average measurements from each location were used to compute the linear relation:

$$K = \frac{p_\infty^{\text{top}} - p_\infty^{\text{bottom}}}{C^{\text{top}} - C^{\text{bottom}}} \tag{5.6}$$

From here on, K, will be referred to as the sensitivity constant. During testing, the change in elevation of the road resulted in approximately a 90 Pa change in ambient pressure. This change in ambient pressure is equivalent to a 7.4 m elevation change. The ambient pressure profile is shown in this chapter's appendix.

5.2.2 Expected Pressure Distributions

XFOIL was used to predict the pressure coefficient distribution on the airfoil shown in Figure 5.3. Once the pressure coefficient distribution was computed, the predicted static pressure, p, was then calculated as a function of freestream velocity squared, U_∞^2, and ambient pressure, p_∞. The ambient pressure acts equally on the entire wing, therefore, it does not produce a pressure differential. To focus on the differences in the pressure distribution that produce aerodynamic forces, only the relative pressure distribution, $p - p_\infty$, was plotted.

In Figure 5.4a, the relative pressure distribution of the top surface is shown for three different freestream velocities. Note that the relative pressure distribution is negative, which means that the pressure is producing an upward force on the top of the wing surface. Integrating the distribution over the entire airfoil results in the aerodynamic forces per unit span of the wing acting on the airfoil. These aerodynamic forces due to pressure can then be decomposed into lift and drag forces. Additionally, the relative pressure distribution changes as the angle of attack varies. Figure 5.4b illustrates the relative pressure distribution for an angle of attack of 5°. Overall, a majority of the relative pressure distribution is more negative, resulting in a larger lift force. It can be seen that both pressure distribution magnitudes also increase with the square of the freestream velocity.

The distributions in Figures 5.4a and 5.4b are well within the region of angles of attack before the airfoil stalls. During stall, the airflow separates from the surfaces, which causes highly dynamic airflow in the separated region. This dynamic instability in the flow consists of vortices and vortex shedding [12] and would be difficult to match a simulation with measured data. Therefore, testing of the pressure sensor array was only performed where airflow is close to steady behavior with minimal separation occurring.

5.2.3 Results

As previously discussed, the pressure sensor array tests were conducted on a slightly inclined road, resulting in changes in ambient pressure. The pressure sensor array measures static pressure, meaning that the changes in ambient pressure affect these measurements. To evaluate the test results, the relative pressure distribution estimates from XFOIL were compared to the measured relative pressure distribution from the barometer, anemometer, and pressure sensor array.

$$C_p \left(\frac{1}{2} \rho v_\infty^2 \right) = p - p_\infty \approx K \Delta C - p_\infty \tag{5.7}$$

The left side of (5.7) is the estimate of the pressure from XFOIL and the right side is the pressure that comes from pressure array measurements.

Figure 5.5a shows results from one of the cells on the sensor array during the test at 0° angle of attack. It is shown that the pressure measurements follow the XFOIL estimate with respect to freestream velocity. The standard deviation is 25.3 Pa while having a decent sensitivity, where the sensitivity constant, K, is 0.46 Pa. Results from the 0° angle of attack

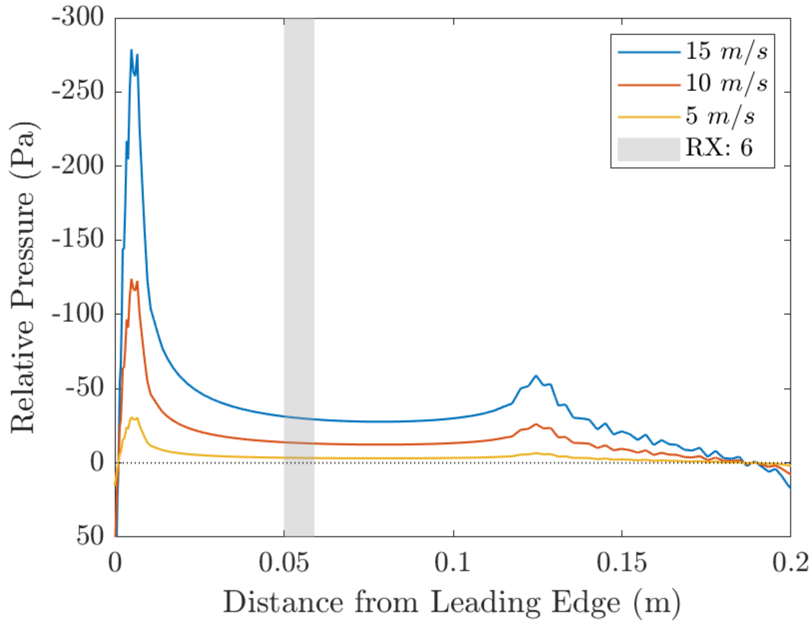

(a) $\alpha = 0°$

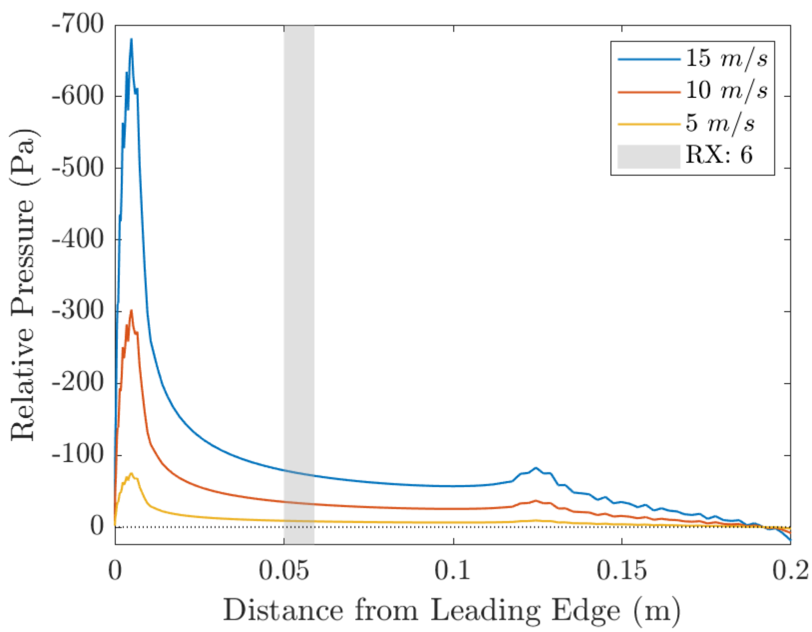

(b) $\alpha = 5°$

Figure 5.4: Relative pressure distribution for the airfoil shown above at (a) 0° and (b) 5° angles of attack flying at 5 m/s, 10 m/s, and 15 m/s according to XFOIL. The RX: 6 cell location is highlighted to show the expected pressure drop for the cell discussed in Section 5.2.3.

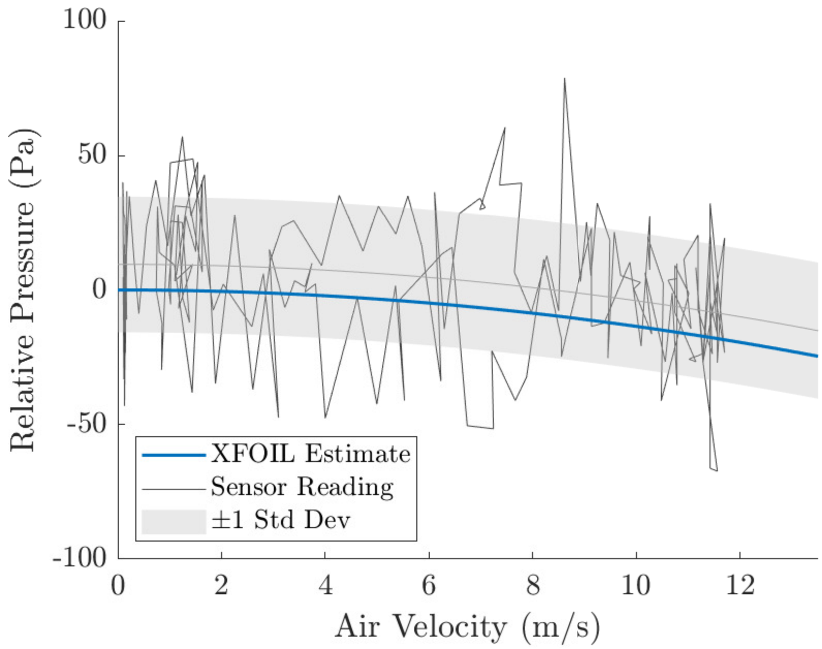

(a) $\alpha = 0°$

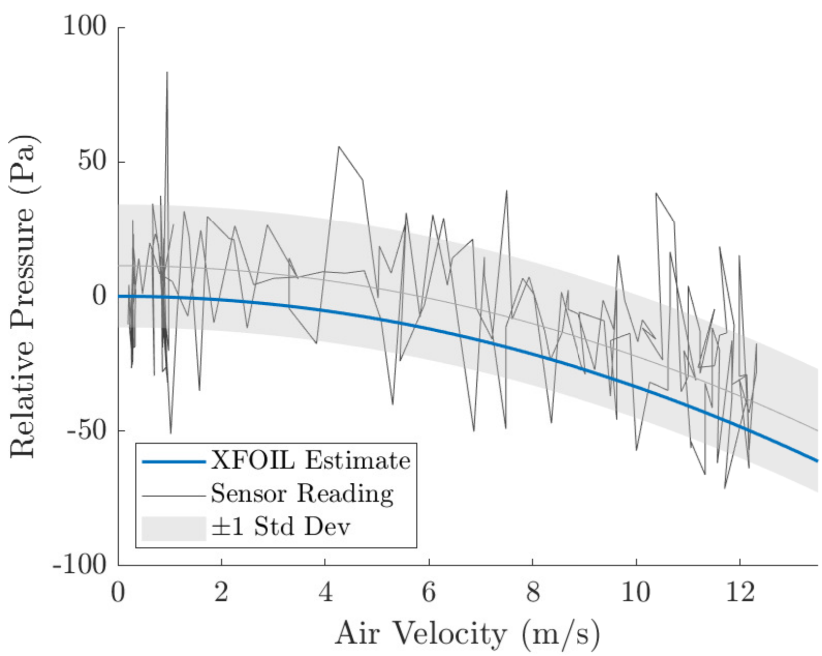

(b) $\alpha = 5°$

Figure 5.5: Comparison between the XFOIL estimated relative pressure and the measured relative pressure at cell, RX: 6 TX: 3, for an angle of attack of (a) 0° and (b) 5°.

test show that more than half of the cells in the sensor array have at most a standard deviation of 55 Pa and more than a fifth of the cells have at most a standard deviation of 35 Pa.

Figure 5.5b illustrates the same element in the sensor array, but at an angle of attack of 5°. It is shown that the pressure sensor measurement also agrees with the pressure estimates from XFOIL. For this cell, at a 5° angle of attack, the standard deviation is 22.9 Pa. As expected, at a higher angle of attack, there is a larger drop in relative pressure. Results from the 5° angle of attack test show that more than half the cells in the sensor array have at most a standard deviation of 45 Pa. Similar plots for the 0° and 5° angle of attack tests were created for the remaining cells in the sensor array. A comprehensive evaluation of all 150 cells is presented in the following section and in Figures 5.8 and 5.9.

5.2.4 Potential for Improving Sensitivity

The sensitivity of the cells can also be improved without lowering bandwidth by averaging their measurements with adjacent cells or by row if similar pressures are expected. In this case, where the pressure sensor array was mounted towards the center of the wing, the rows of cells are measuring very similar pressures, therefore they can be averaged. Figure 5.6

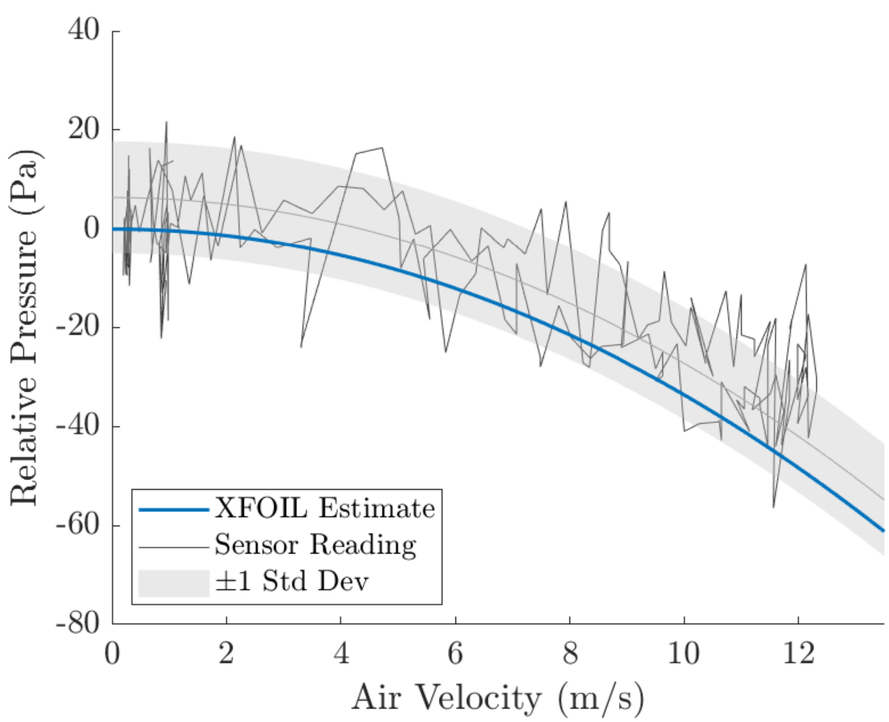

Figure 5.6: The pressure average on the entire RX: 6 row for an angle of attack of 5°. If the pressure distribution is assumed to be constant over a section of cells, then they can be averaged to reduce the standard deviation.

shows the average of the entire row of cells, which also contained cell RX: 6, TX: 3. The standard deviation dropped to only 10.6 Pa. It is important to note that this cannot be done closer to the wingtip as the pressure loss in the spanwise direction is significant. Another way to improve sensitivity is by optimizing the design of the sensor.

5.2.4.1 Cell Quality

The sensitivity of the cells in the pressure sensor array is represented by each cell's sensitivity constant, K. The values that are larger are more sensitive, since the same change in pressure will result in a larger percent change in capacitance. However, it is important to take into consideration noise of the sensor. If a sensitive cell has a large amount of noise, variance in measured pressure will be large. A good cell will have both high sensitivity and low noise. To qualitatively inspect the array, a metric defined as the normalized ratio of variance over K, is used in Figure 5.7. Lower values define better cells.

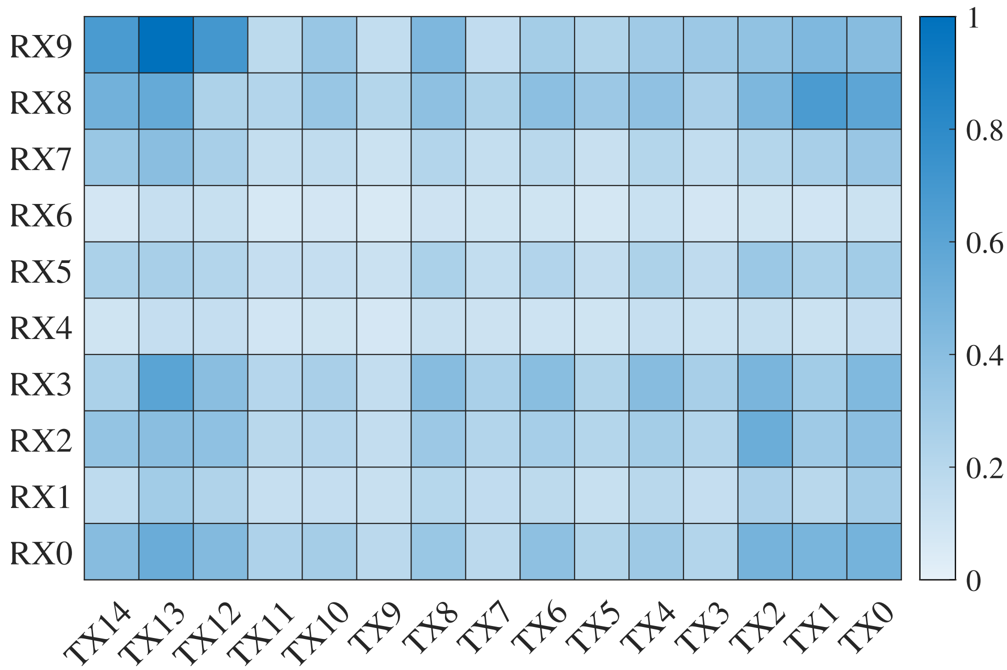

Figure 5.7: The normalized ratio of the variance over the sensitivity constant, K, of each cell is mapped. Better sensors register lower numbers with this metric. The top row, RX: 9, is closest to the leading edge, while the bottom row, RX: 0, is closest to the trailing edge.

The metric was then used to prevent bad cells from deteriorating averaged results. A threshold of 0.45 for the ratio of the variance over K, was chosen empirically. This threshold only skipped over 15 cells, which were not included in the averaging. The results from the $0°$ and $5°$ angle of attack tests were averaged in the spanwise direction at $11.5 \pm 0.2\ m/s$ and $12 \pm 0.2\ m/s$, respectively. These averages were compared to XFOIL predictions in Figures 5.8 and 5.9.

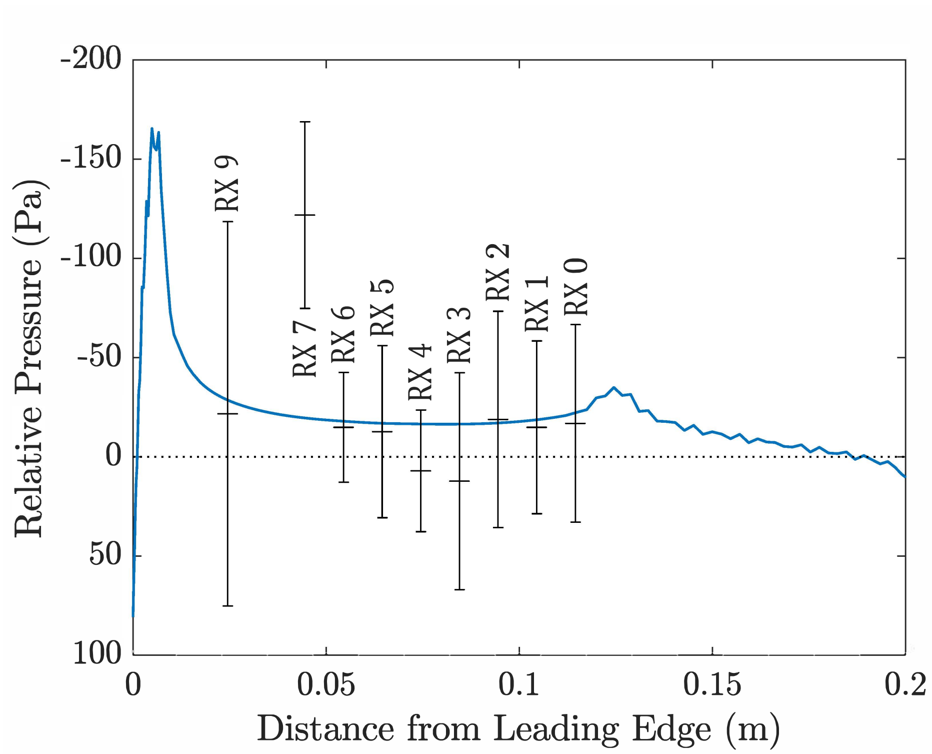

Figure 5.8: Relative pressure distribution for the airfoil at 0° angle attack with a freestream velocity of 11.5 m/s. The sensor measurements within ±0.2 m/s for each row were averaged and plotted with a ±1 standard deviation range. RX: 8 has a large error for this test and is not captured in the range of the relative pressure range plotted.

The measurements correlate with XFOIL estimates well, with the exception of the second and third rows, RX: 7 and 8, in the 0° angle of attack test. It is hypothesized that there was some stray capacitance which caused a drift in calibration.

5.3 Optimized Sensor Design

To be usable as part of the control shown in Chapter 4, the pressure sensors were optimized to be more sensitive. Getting the capacitive pressure sensors to be more sensitive, there are a two improvements made on the preliminary thin-film capacitive pressure design. Additionally, the design would be manufactured on a flex-PCB to be able to conform to a more efficient airfoil.

The first design change was to the membrane of the sensor. Rather than being 1 $cm \times 1\ cm$, the membrane was expanded to 1.5 $cm \times 1.5\ cm$. This reduces the stiffness of the membrane so the same pressure drop results in a greater deflection of the membrane.

The second design change was to optimize the traces of the sensor so that the same change in pressure results in the maximal change in capacitance. To increase the change

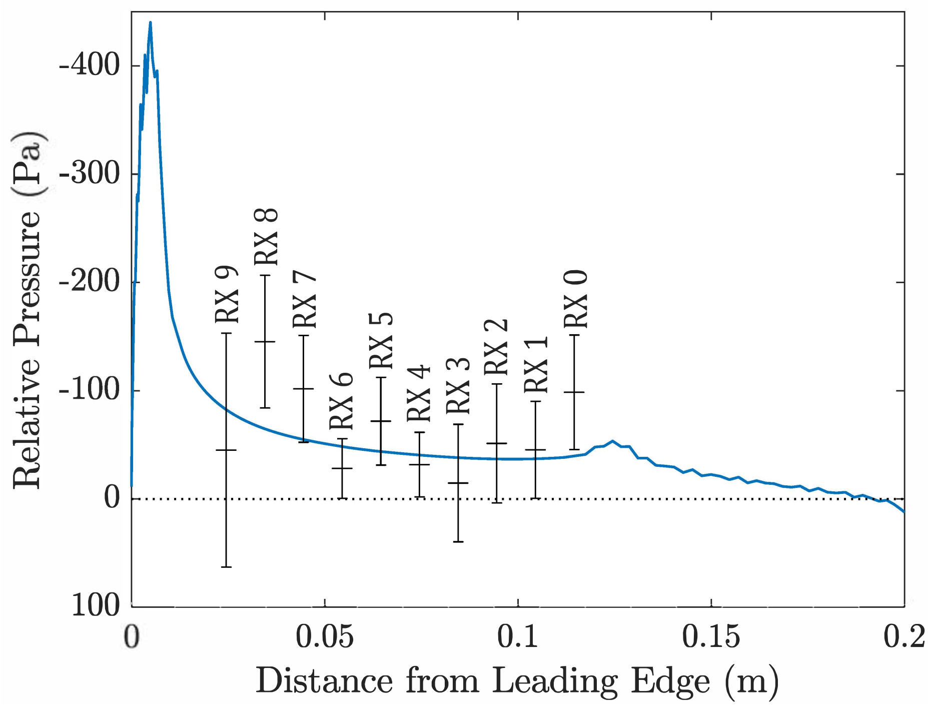

Figure 5.9: Relative pressure distribution for the airfoil at 5° angle attack with a freestream velocity of 12 m/s. The sensor measurements within ±0.2 m/s for each row were averaged and plotted with a ±1 standard deviation range.

in capacitance, a design that changes the electric field gradient the most, must be utilized. As explored in previous works, the electric potential field gradient can be increased by increasing the edges of the traces through the use of finger-like designs [33, 31]. Therefore, an axi-symmetric design was developed and optimized through the use of a grid search of the design's parameters - rather than using parallel fingers, concentric sets of circles were used.

5.3.1 Optimized Sensor Analysis

The optimal pressure sensor was designed for a 10 Pa drop in pressure. Using an FEA tool, the center of the aluminized Mylar membrane was computed to have a 4.7 μm deflection for the pressure drop. With the deflection profile from the FEA tool, another FEA analysis was run for the various parameters of the design.

The axi-symmetric design had several parameters as noted in Figure 5.10. Searching over possible parameter values, the trace width of the finger and the outside ring width was noticed to have little effect to the capacitance change, so they were chosen for robustness of the design and manufacturability. This design was for a flex-PCB, so the outside ring was

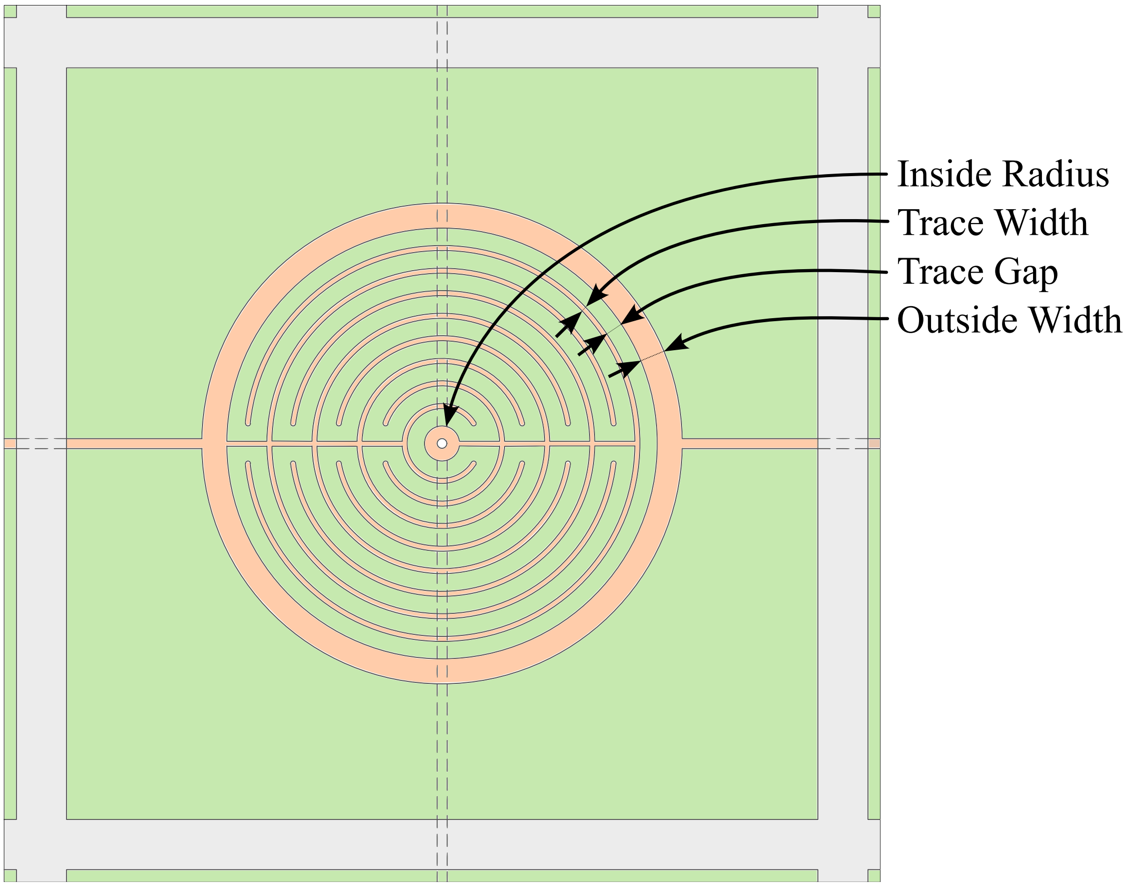

Figure 5.10: The to-scale optimized capacitive pressure sensor design with the parameters labeled. The outer-most ring and the connected traces are the drive traces, and the inner-most via and connected traces are the sense traces. There are 4 sets of rings shown here.

chosen to be 0.5 mm to prevent cracking of the trace, while the finger width was chosen to be 0.1 mm. The center radius on the other hand was more optimal for the design if it were smaller, so the smallest size of via was used - the via connected the inside trace to the rest of the sensor array. The other parameters, number of ring sets and gap between traces, were varied and compared to choose the largest change in capacitance. The final design is shown in Figure 5.10.

Figure 5.11a shows the percent change in capacitance for the 10 Pa drop in pressure. It shows that the best design choice was a design with the least number of ring sets and the largest possible gap between traces. However, this result fails to take into consideration stray capacitance from the PCB that comes from routing the traces near other traces. The stray capacitance can reduce the change in capacitance by the relation:

$$\Delta C\% = \frac{\delta C}{C_0 + C_{\text{stray}}} \tag{5.8}$$

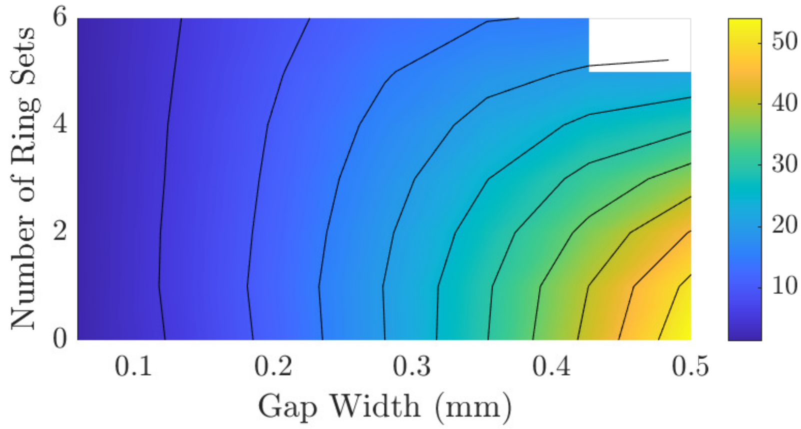

(a) No stray capacitance

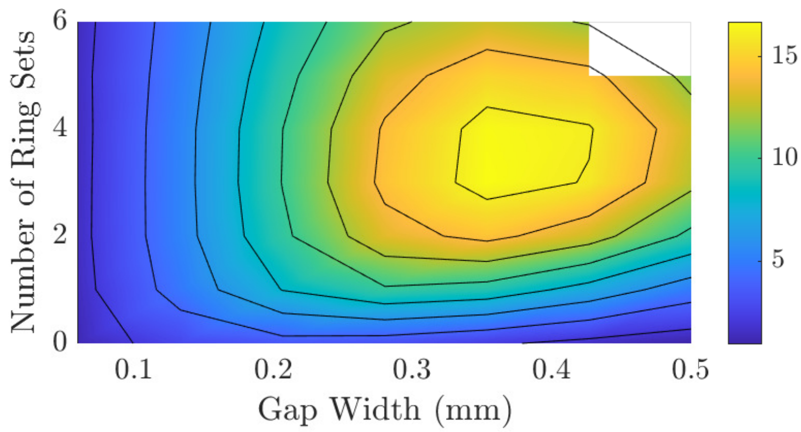

(b) 50 fF of stray capacitance

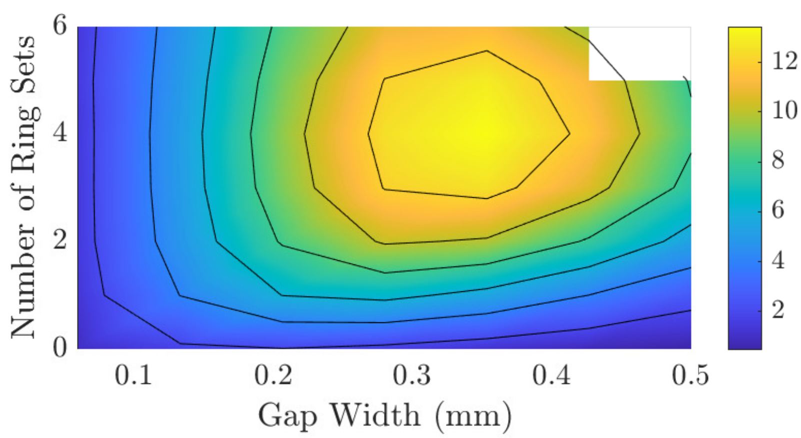

(c) 100 fF of stray capacitance

Figure 5.11: The percent change in capacitance with a 10 Pa drop in pressure.

If the design does not have a large nominal capacitance, C_0, then stray capacitance can drastically vary the percent change in capacitance. Varying amounts of stray capacitance were explored and the results can be seen in Figures 5.11b and 5.11c. The optimal parameter values are now towards the center of the design space. Consequently, the capacitance pressure sensor design was chosen to have 4 sets of rings and a trace gap width of 0.35 mm.

5.3.2 Optimized Sensor Tests

The new sensor design was then tested with a 150 Pa pressure drop. The results of the optimized pressure sensor are shown in Figure 5.12. This result is from one of the better sensors in the array that was compared to the same pressure sensor as before, the LPS25H from STMicroelectronics. The test was conducted for 30 seconds, after which the capacitance sensors seem to have drifted. The noise for the pressure sensor was improved from the previous design - the standard deviation of 25 Pa was improved to a standard deviation of 20 Pa. This is larger than that of the pressure sensors used in Chapters 3 and 4, but this can potentially be overcome by using more sensors for each wing section.

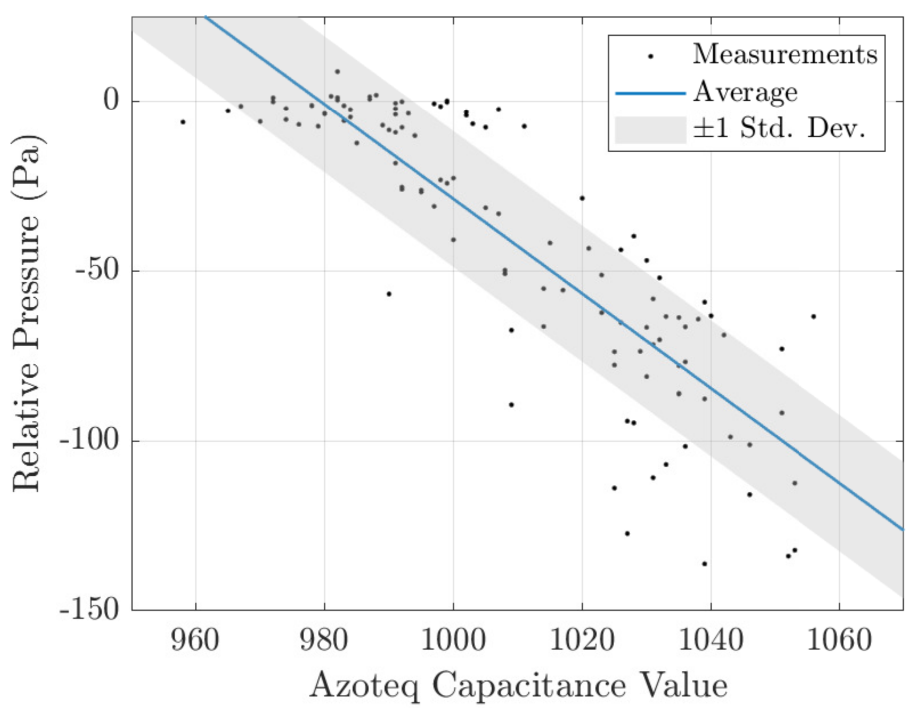

Figure 5.12: The output of one of the better capacitive pressure sensors for a 150 Pa pressure drop. The noise was measured to have a standard deviation of 20 Pa.

5.4 Concluding Remarks

The distributed capacitive pressure sensor array presented in this chapter demonstrated its ability to measure small quasi-static pressure distribution changes across an aerodynamic surface. The optimized pressure sensor design was able to obtain a resolution of 20 Pa. This resolution was obtained while the entire array was being measured every 150 ms, which translates to a 1 ms time/cell update rate.

5.4.1 Sensor Limitations

Some limitations were observed while testing the capacitive pressure sensor array. The first observation was that the colder outside temperature had an effect on the sealed cells. Testing in colder weather caused the air inside of the cells to shrink and show higher initial capacitances. The second observation was that close proximity to another object may change the capacitance of the cells. Luckily, for aerial vehicles, close proximity to another object is not a concern during flight. However, this may affect the usability of this sensor when utilized in another application where other objects may be close by.

5.4.2 Future work

Manufacturing variability needs to be reduced by using more uniform bonding technology such as thermoplastic welding, rather than a pressure sensitive adhesive which may have stability issues. With improvements in sensor manufacturing consistency, the sensor array can be used with the work from previous chapters to sense localized airflow disturbances and allow the control of the airplane with a less intrusive distributed pressure sensor array.

Appendix

Figures 5.13 and 5.14 are the test condition profiles. Both tests for 0° and 5° angle of attack were conducted on the road in the direction of decreasing elevation.

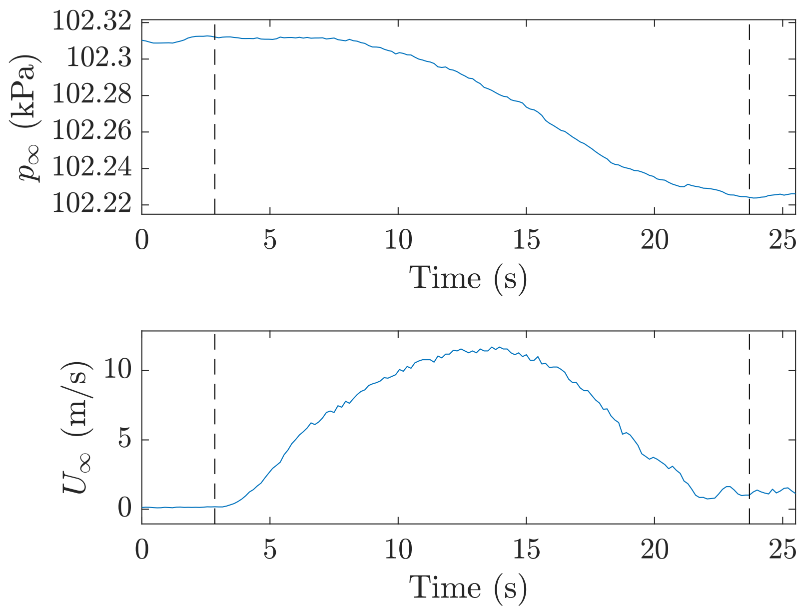

Figure 5.13: The ambient pressure profile and freestream velocity for the test at a 0° angle of attack.

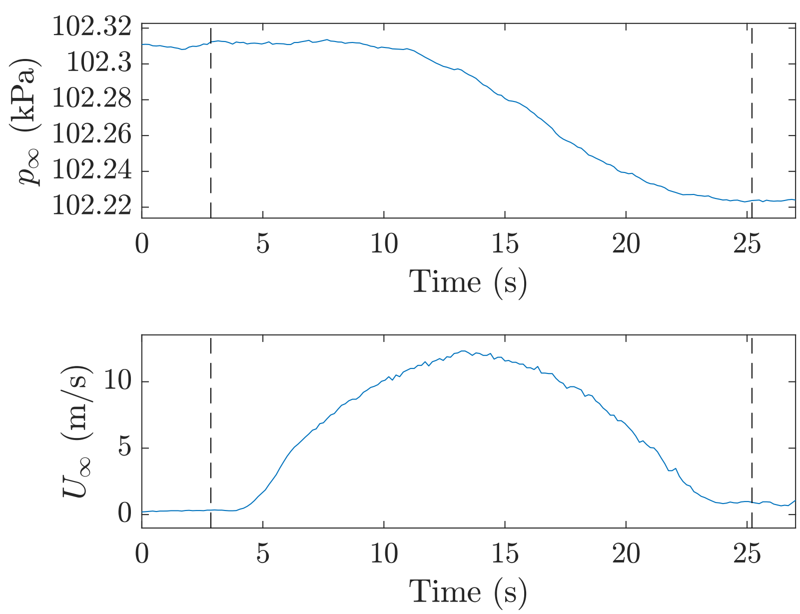

Figure 5.14: The ambient pressure profile and freestream velocity for the test at a 5° angle of attack.

Chapter 6

Conclusion

In this dissertation, a method to measure the pressure distribution, analyze the airflow, and control an airplane through the use of distributed pressure sensors across sections of a wing was introduced. Chapter 2 compared three methods used to retrieve the 2 dimensional aerodynamic parameters of angle of attack and freestream velocity from distributed pressure sensors over the chord of the airfoil. The Unscented Kalman Filter was chosen due to its faster compute time and higher accuracy. Chapter 3 then explains how the Unscented Kalman Filter was utilized to retrieve the aerodynamic parameters during wind tunnel testing. These two chapters demonstrated how the use of an Unscented Kalman Filter with a zero-dynamics model and the use of the coefficient of pressure from a viscid XFOIL analysis was able to estimate the parameters well. The UKF was able to accurately compute estimates in about 1 ms for all conditions tested. It was also observed that the accuracy of the estimates improved as the velocity of airflow was increased. Chapter 4 then combined the findings from Chapters 2 and 3 to introduce a control scheme that utilized the estimates of the airflow on all sections of wing to control the attitude of an airplane. This control scheme took advantage of distributed pressure sensors to optimally adjust actuators (i.e. flaps) across the wing sections accordingly. The performance of this control scheme was also proved with roll attitude tests, where the new controller was able to more efficiently track a reference signal as well as better reject a localized airflow disturbance when compared to a traditional controller. Last, Chapter 5 explored an innovative method to develop and manufacture sensitive, thin-film, capacitive pressure sensors which could be applied to aerodynamic surfaces to measure the pressure distribution across a wing. The potential for such technology was illustrated as an improvement as the current design utilizing COTS sensors, which are intrusive to the structure of the wing. Implementing thin film capacitive pressure sensors allows for the retrieval of 2 dimensional airflow parameter estimates to be performed on multiple discretized sections of the wing with little to no wing structure intrusion.

6.1 Future Work

There are two foreseeable areas that have the potential for future work based on the experiments conducted for this dissertation. The first area is in the space of thin-film capacitive sensors. As noted in Chapter 5, the design presented had a large variability in manufacturing quality. Utilizing such a thin film pressure sensor over a COTS pressure sensor would improve the performance of the airplane as the structure would not need to be modified, and consequently made heavier. Therefore, rather than accommodating the pressure sensors inside the wing, they could be applied topically to the wing surface.

The second area that could be explored is improving the method for checking for bad estimates. During the tests conducted for this dissertation, there were a few failed pressure sensors that drove the estimates away from the actual values of the aerodynamic parameters. If the turbulence in the environment is characterized, each sensor reading could then be compared adjacent sensors to prevent the controller from using bad estimates.

Bibliography

[1] *A microcontroller by Raspberry Pi.* RP2040. Raspberry Pi Ltd. 2020.

[2] Gianluca Amendola, Ignazio Dimino, Marco Magnifico, Rosario Pecora, et al. "Numerical design of an adaptive aileron". In: *Sensors and Smart Structures Technologies for Civil, Mechanical, and Aerospace Systems 2016.* Vol. 9803. SPIE. 2016, pp. 675–693.

[3] John David Anderson Jr. "Fundamentals of Aerodynamics". In: Tata McGraw-Hill Education, 2010. Chap. 3, pp. 207–210.

[4] John David Anderson Jr. "Fundamentals of Aerodynamics". In: Tata McGraw-Hill Education, 2010. Chap. 5, pp. 415–420.

[5] *Barometric Pressure Sensor, with stainless steel cap.* MS5607-02BA03. TE Connectivity. Nov. 2020.

[6] Randal W Beard and Timothy W McLain. "Small unmanned aircraft: Theory and practice". In: Princeton university press, 2012. Chap. 6, pp. 95–97.

[7] R. A. Boie. "Capacitive impedance readout tactile image sensor". In: *IEEE Int. Conf. on Robotics and Automation.* Vol. 1. 1984, pp. 370–378. DOI: 10.1109/ROBOT.1984.1087186.

[8] Kasper Trolle Borup, Thor Inge Fossen, and Tor Arne Johansen. "A machine learning approach for estimating air data parameters of small fixed-wing UAVs using distributed pressure sensors". In: *IEEE Transactions on Aerospace and Electronic Systems* 56.3 (2019), pp. 2157–2173.

[9] Sergio Callegari, Michele Zagnoni, A Golfarelli, M Tartagni, A Talamelli, P Proli, and A Rossetti. "Experiments on aircraft flight parameter detection by on-skin sensors". In: *Sensors and Actuators A: Physical* 130 (2006), pp. 155–165.

[10] Mark Drela and Harold Youngren. "Xfoil subsonic airfoil development system". In: *Open source software available at: http://web. mit. edu/drela/Public/web/xfoil* (2008).

[11] Ronald S Fearing. "Tactile sensing mechanisms". In: *The International Journal of Robotics Research* 9.3 (1990), pp. 3–23.

[12] Mark A Feero, Philippe Lavoie, and Pierre E Sullivan. "Influence of synthetic jet location on active control of an airfoil at low Reynolds number". In: *Experiments in Fluids* 58.8 (2017), pp. 1–12.

[13] Nikola Gavrilovic, Murat Bronz, Jean-Marc Moschetta, and Emmanuel Bénard. "Bioinspired wind field estimation—part 1: Angle of attack measurements through surface pressure distribution". In: *International Journal of Micro Air Vehicles* 10.3 (2018), pp. 273–284.

[14] Bonnie L Gray and Ronald S Fearing. "A surface micromachined microtactile sensor array". In: *IEEE Int. Conf. on Robotics and Automation*. Vol. 1. 1996, pp. 1–6.

[15] Alexander Gruebele, Jean-Philippe Roberge, Andrew Zerbe, Wilson Ruotolo, Tae Myung Huh, and Mark R Cutkosky. "A stretchable capacitive sensory skin for exploring cluttered environments". In: *IEEE Robotics and Automation Letters* 5.2 (2020), pp. 1750–1757.

[16] Zhanat Kappassov, Juan-Antonio Corrales, and Véronique Perdereau. "Tactile sensing in dexterous robot hands". In: *Robotics and Autonomous Systems* 74 (2015), pp. 195–220.

[17] Suhan Kim, Regan Kubicek, Aleix Paris, Andrea Tagliabue, Jonathan P How, and Sarah Bergbreiter. "A whisker-inspired fin sensor for multi-directional airflow sensing". In: *IEEE/RSJ Int. Conf. on Intelligent Robots and Systems (IROS)*. 2020.

[18] Maarja Kruusmaa, Paolo Fiorini, William Megill, Massimo De Vittorio, Otar Akanyeti, Francesco Visentin, Lily Chambers, Hadi El Daou, Maria-Camilla Fiazza, Jaas Ježov, et al. "Filose for svenning: A flow sensing bioinspired robot". In: *IEEE Robotics & Automation Magazine* 21.3 (2014), pp. 51–62.

[19] Jayanth N Kudva. "Overview of the DARPA smart wing project". In: *Journal of intelligent material systems and structures* 15.4 (2004), pp. 261–267.

[20] Juliana P Leitzke, Astrid Della Mea, Lisa-Marie Faller, Stephan Mühlbacher-Karrer, and Hubert Zangl. "Wireless differential pressure measurement for aircraft". In: *Measurement* 122 (2018), pp. 459–465.

[21] Matthew R Maschmann, Ben Dickinson, Gregory J Ehlert, and Jeffery W Baur. "Force sensitive carbon nanotube arrays for biologically inspired airflow sensing". In: *Smart Materials and Structures* 21.9 (2012), p. 094024.

[22] A Mohamed, S Watkins, A Fisher, M Marino, K Massey, and R Clothier. "Bioinspired wing-surface pressure sensing for attitude control of micro air vehicles". In: *Journal of Aircraft* 52.3 (2015), pp. 827–838.

[23] Abdulghani Mohamed, Simon Watkins, Reece Clothier, M Abdulrahim, K Massey, and R Sabatini. "Fixed-wing MAV attitude stability in atmospheric turbulence—Part 2: Investigating biologically-inspired sensors". In: *Progress in Aerospace Sciences* 71 (2014), pp. 1–13.

[24] Mehran Motamed and Joseph Yan. "A review of biological, biomimetic and miniature force sensing for microflight". In: *2005 IEEE/RSJ International Conference on Intelligent Robots and Systems*. IEEE. 2005, pp. 3939–3946.

[25] Omnexus. “Polymer Young’s Modulus Repo”. In: *URL https://omnexus.specialchem.com/polymer-properties/properties/young-modulus* ().

[26] Aditya A Paranjape, Jinyu Guan, Soon-Jo Chung, and Miroslav Krstic. “PDE boundary control for flexible articulated wings on a robotic aircraft”. In: *IEEE Transactions on Robotics* 29.3 (2013), pp. 625–640.

[27] Steve Park, Hyunjin Kim, Michael Vosgueritchian, Sangmo Cheon, Hyeok Kim, Ja Hoon Koo, Taeho Roy Kim, Sanghyo Lee, Gregory Schwartz, Hyuk Chang, et al. “Stretchable energy-harvesting tactile electronic skin capable of differentiating multiple mechanical stimuli modes”. In: *Advanced Materials* 26.43 (2014), pp. 7324–7332.

[28] Joseph M Romano, Kaijen Hsiao, Günter Niemeyer, Sachin Chitta, and Katherine J Kuchenbecker. “Human-inspired robotic grasp control with tactile sensing”. In: *IEEE Transactions on Robotics* 27.6 (2011), pp. 1067–1079.

[29] Cameron J Rose, Parsa Mahmoudieh, and Ronald S Fearing. “Modeling and control of an ornithopter for diving”. In: *2016 IEEE/RSJ International Conference on Intelligent Robots and Systems (IROS)*. IEEE. 2016, pp. 957–964.

[30] Taavi Salumäe and Maarja Kruusmaa. “Flow-relative control of an underwater robot”. In: *Proceedings of the Royal Society A: Mathematical, Physical and Engineering Sciences* 469.2153 (2013), p. 20120671.

[31] Ethan W Schaler, Loren Jiang, Caitlyn Lee, and Ronald S Fearing. “Bidirectional, Thin-Film Repulsive-/Attractive-Force Electrostatic Actuators for a Crawling Milli-Robot”. In: *2018 International Conference on Manipulation, Automation and Robotics at Small Scales (MARSS)*. IEEE. 2018, pp. 1–8.

[32] Bryan E Schubert, Andrew G Gillies, and Ronald S Fearing. “Angled microfiber arrays as low-modulus, low Poisson’s ratio compliant substrates”. In: *Journal of Micromechanics and Microengineering* 24.6 (2014), p. 065016.

[33] BG Sheeparamatti, Prashant D Hanasi, Vanita Aibbigeri, and Naveen Meti. “Study of capacitance in electrostatic comb-drive actuators”. In: *Excerpt from the Proceedings of the COMSOL Conference in Pune*. 2015.

[34] He Shen, Yunjun Xu, and Benjamin T Dickinson. “Micro air vehicle’s attitude control using real-time pressure and shear information”. In: *Journal of Aircraft* 51.2 (2014), pp. 661–671.

[35] He Shen, Yunjun Xu, and Charles Remeikas. “Pitch control of a micro air vehicle with micropressure sensors”. In: *Journal of Aircraft* 50.1 (2013), pp. 239–248.

[36] Hidetoshi Takahashi, Kiyoshi Matsumoto, and Isao Shimoyama. “Measurement of differential pressure on a butterfly wing”. In: *2010 IEEE 23rd Int. Conf. on Micro Electro Mechanical Systems (MEMS)*. 2010, pp. 63–66.

[37] Ardupilot Development Team. *Ardupilot*. URL: `http://ardupilot.org`.

[38] *VelociCalc 8346 anemometer*. 8346. TSI. Nov. 2002.

[39] Kieran T Wood, Sergio Araujo-Estrada, Thomas Richardson, and Shane Windsor. "Distributed Pressure Sensing–Based Flight Control for Small Fixed-Wing Unmanned Aerial Systems". In: *Journal of Aircraft* 56.5 (2019), pp. 1951–1960.

[40] Yong Xu, Fukang Jiang, Scott Newbern, Adam Huang, Chih-Ming Ho, and Yu-Chong Tai. "Flexible shear-stress sensor skin and its application to unmanned aerial vehicles". In: *Sensors and Actuators A: Physical* 105.3 (2003), pp. 321–329.